

Deformation of a planar ferromagnetic elastic ribbon

G. R. Krishna Chand Avatar · Vivekanand Dabade

Received: date / Accepted: date

Abstract While extensive studies have been conducted on purely elastic ribbons, in this paper we explore the influence of magnetisation on the deformation of planar ferromagnetic elastic ribbons. We begin the investigation by deriving the leading-order magnetic energy associated with a curved planar ferromagnetic elastic ribbon. The sum of the magnetic and the elastic energy is the total energy of the ribbon. We derive the equilibrium equations by taking the first variation of the total energy. We then systematically determine and analyse solutions to these equilibrium equations under various canonical boundary conditions. We also analyse the stability of the equilibrium solutions. Comparing our findings with the well-studied Euler's Elastica provides insights into the magnetic effects on the deformation behaviour of elastic ribbons. Our analysis contributes to a deeper understanding of the interplay between magnetisation and the mechanical response of planar ferromagnetic structures, and offers valuable insights for both theoretical and practical applications.

Keywords Magnetoelastic slender structures · Soft ferromagnets · Hard ferromagnets · Ribbons · Elastica

Mathematics Subject Classification (2020) MSC code1 · MSC code2 · more

1 Introduction

Magneto-elastic slender structures exhibit complex coupling between magnetism and deformation or elasticity. A fascinating experiment conducted in the late 1960s demonstrated the intriguing connection between deformation and magnetism in a mechanical spring that carries an electric current and is placed in an external magnetic field, see Fig. 1. Under the influence of a tensile load, the spring undergoes buckling, underscoring the complexity of this coupling phenomenon. Slender ferromagnetic structures offer the potential to achieve substantial deformations using remote external magnetic fields. This complex coupling is being applied in ferromagnetic continuum robots, innovative actuators, and remotely controlled minimally invasive surgeries, [14, 21].

Purely magnetic slender structures [8] and purely elastic slender structures [2] have each been studied separately in great detail. The study of elastic slender structures dates back to Euler, who obtained the deformation of an elastic planar rod. These deformations are represented by a family of planar curves using elliptic functions and is known as Euler's Elastica. Elastica finds applications ranging from the modelling of DNA loops to laying of ocean cables and design of elastic robots, see [3, 5, 11, 1]. There have also been fairly recent studies concerning the stability of the solutions to the Elastica, see [17] and [15].

Vivekanand Dabade
Department of Aerospace Engineering
Indian Institute of Science
Bengaluru, India
E-mail: dabade@iisc.ac.in

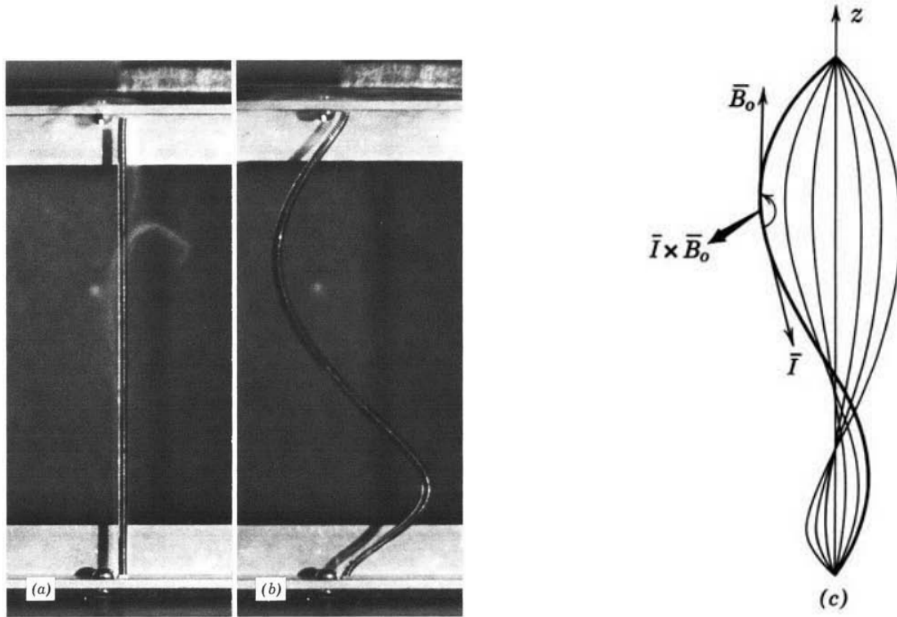


Fig. 1: (a) A conducting spring, elongated between the poles of a electromagnet, serves as the experimental configuration. (b) The onset of instability occurs after the electromagnet is turned on. (c) Schematic of the first mode of instability. Here, I is the current flowing through the spring and \mathbf{B}_o is the magnetic flux density due to the electromagnet. Note that the spring buckles under tensile force. Source: [26].

Similarly, there have been extensive studies on ferromagnetic thin films and straight rods in the field of micromagnetics, [8,23]. Micromagnetics is a continuum theory for magnetism that has proven to be a robust model capable of explaining and predicting the diverse array of domain structures observed in ferromagnetic materials. These studies consider the ferromagnetic slender structure without deformation and delineate the role of aspect ratio on the formation of the observed magnetic domain structures. The magnetisation vector $\mathbf{m}(\mathbf{x})$ is the primary variable in the micromagnetics functional. $\mathbf{m}(\mathbf{x})$ is a unit-normed vector supported on a ferromagnetic body. The micromagnetic functional is expressed as the sum of exchange, magnetocrystalline anisotropy, magnetostatic (abbreviated as demag.), and Zeeman energy, [7]. In particular, the demag. energy, strongly depends on the shape of the body and is computed by solving Maxwell's equations of magnetostatics. The demag. energy is computationally expensive and is difficult to calculate for general 3D bodies but takes simpler forms for slender structures. This gives us an opportunity to explore these problems (semi-) analytically and hence, the demag. energy will play a crucial role in our analysis.

There has been limited research dedicated to understand the coupling between magnetisation and deformation in thin ferromagnetic structures. Bulk ferromagnetic solids (Iron, Nickel, Galfenol etc.) are known to deform when magnetised. This phenomenon is known as Joule magnetostriction. However, even under strong external magnetic fields, magnetostriction strains are small, typically in the order of 10^{-5} . Our work does not consider Joule magnetostriction, we are primarily interested in understanding the deformation in slender ferromagnetic structures due to the effects of demag. energy and Zeeman energy. The elastic energy and magnetic energy are comparable in slender ferromagnetic structures, even though the elastic energy density is typically much greater than the magnetic energy density in bulk ferromagnetic materials. Hence, we can obtain large displacements in ferromagnetic slender structures while the strains in bulk ferromagnetic solids due to Joule magnetostriction are very small.

In bulk ferromagnetic materials, the elastic energy density scales as E ($\sim 10^{11} J/m^3$), whereas the demag. energy scales as K_d ($\sim 10^5 J/m^3$). Here, K_d and E represent the magnetostatic energy constant and Young's

modulus of the material, respectively, with both being material parameters. However, in slender structures the elastic energy and the demag. energy density scale very differently with respect to the aspect ratio. The leading-order demag. energy of a slender ferromagnetic ribbon scales as $\mathcal{O}(K_d a t l)$, and the elastic energy scales as $\mathcal{O}\left(\frac{E I}{2l}\right)$. Here, thickness, width, and length of the ferromagnetic ribbon are denoted as t , a , and l , respectively, and $I = \frac{b t^3}{12}$, is the area moment of inertia, see Fig 2. Hence, ferromagnetic slender structures offer an opportunity to tune the aspect ratio, allowing the interaction between demag. energy and elastic energy. A balance of these energies implies that our analysis is valid for ribbons with an aspect ratio of $\mathcal{O}\left(\sqrt{\frac{E}{24K_d}}\right)$.

In our article, we explore the interaction between elasticity and magnetism in the simplest setting. Our analysis focuses on the deformation of a slender body resulting from the interplay of demag. energy and Zeeman energy, collectively referred to as magnetic energy, along with elastic energy. We consider a ferromagnetic ribbon, that is, a planar ribbon or rod composed of a ferromagnetic material such as Iron or Nickel. In particular, we shall study the two following cases:

- *Case 1. (Soft ferromagnet)*: Magnetisation vector $\mathbf{m}(\mathbf{x})$ is spatially constant and does not change with deformation. This case characterises soft ferromagnetic materials such as Permalloy, with an external magnetic field large enough to saturate the magnetisation uniformly throughout the deformed planar ribbon.
- *Case 2. (Hard ferromagnet)*: Magnetisation vector $\mathbf{m}(\mathbf{x})$ makes a constant angle with respect to the tangent of the deformed planar curve. Here, the tangent vector, and hence the magnetisation vector vary spatially as the slender body undergoes deformation. This case characterises hard ferromagnetic materials such as Neodymium or Samarium-Cobalt.

The total energy of a ferromagnetic slender ribbon is given by the sum of the elastic energy, magnetic energy of the ribbon and energy due to mechanical loading device. We shall consider the ribbon to be inextensible and hence the elastic energy is given by its bending energy. The magnetic energy is formulated based on the principles of micromagnetics. The magnetic energy is equal to the sum of the demag. energy and the Zeeman energy. We obtain the demag. energy for a curved ferromagnetic ribbon by employing a local material frame aligned with the tangent line of the deformed curve. Working in the deformed configuration alleviates the need to define a pull-back for the magnetisation vector $\mathbf{m}(\mathbf{x})$ and solving the Maxwell's equations of magnetostatics in the reference configuration. Various pullbacks for magnetisation are defined in the literature, posing challenges in the rational selection of the appropriate one, [12, 13]. The leading order demag. energy is local in nature and hence amenable for analysis. Calculating the remaining component of the magnetic energy, namely the Zeeman energy of the ribbon, is straightforward.

We determine the deformed configuration by solving the equilibrium equations obtained by taking the first variation of the total energy. The equilibrium equations show that the magnetisation produces a body couple along the length of the curve that is dependent on the local orientation of the curve, in addition to the conventional terms originating from elastic energy, see Eqn. 25. The equilibrium equations are solved numerically for various canonical boundary conditions, using AUTO-07p, a standard software used in continuation and bifurcation problems [9, 10]. Further, we also perform a stability analysis of our computed solutions. The stability analysis involves casting the second variation of the total energy as a Sturm-Liouville boundary value problem. The eigenvalues of this boundary value problem, as the load is varied continuously, are used to determine the stability of the deformed configurations.

We obtain the equilibrium path and the stability of the first few relevant modes, under quasi-static load control simulation. Our results provide us with a stable deformed state of the ferromagnetic ribbon, beginning from zero load and, in certain instances, a moderate tensile load, and extending to an arbitrarily large compressive load. The main findings from our analysis are as follows:

Case 1: Soft ferromagnetic ribbon:

- Critical buckling load is determined to be tensile under all canonical boundary conditions. Refer to Figs. 10, 11 and 12.
- Fixed-fixed boundary conditions reveal the emergence of novel stable curves on the mode-2 branch. In Fig. 11(a), we highlight the segment of the mode-2 branch that corresponds to novel stable configurations, observed in a ferromagnetic ribbon but absent in Euler's Elastica. A novel stable mode shape featuring two self-intersection points is shown in red in Fig. 11 (a), and additional illustrations can be found in Fig. 11 (b).

Case 2: Hard ferromagnetic ribbon:

- Introduction of magnetization leads to an increase in the compressive buckling load compared to the Elastica. See Figs.13, 14 and 15.
- Comparing the deformed configuration of the hard ferromagnetic ribbon to Euler's Elastica, no discernible difference in shape is observed, despite the presence of a change in the vertical reaction force at the supports. The expressions for the vertical reaction forces at the supports are provided in Equations 75 and 76.

1.1 Organisation of the paper

The paper is organised as follows: In Section 2, we present the mathematical model for the ferromagnetic planar ribbon. Beginning with the geometry and kinematics, we then derive the total energy of soft and hard ferromagnetic planar ribbons. We conclude this section with the derivation of the equilibrium equations for various canonical boundary conditions. In Section 3, we describe the numerical continuation method employed for solving the equilibrium equations. Section 4, focuses on the stability analysis of the solutions to the equilibrium equations. Section 5 details the numerical solutions for various canonical loading scenarios. We comprehensively analyse the deformation behaviour and bifurcation patterns for various canonical loading scenarios. The end of Section 5 is devoted to a discussion in the limit as \bar{K}_d approaches infinity. Here, \bar{K}_d represents the ratio of the magnetostatic energy density to the elastic energy density of the ferromagnetic ribbon. We close our paper with the conclusions and remarks in Section 6.

2 One-dimensional model for a ferromagnetic ribbon

2.1 Kinematics of ribbons

Ribbons are characterized by three disparate length scales – length (l), width (a), thickness (t) – such that $t \ll a \ll l$. Geometrically, ribbon is described in terms of a three-coordinate set – centerline arc length (s), lateral (\tilde{a}), transverse (\tilde{t}) coordinates. In the reference configuration, the ribbon is represented in standard basis of $(\mathbf{e}_1, \mathbf{e}_2, \mathbf{e}_3)$ as $s\mathbf{e}_3 + \tilde{a}\mathbf{e}_1 + \tilde{t}\mathbf{e}_2$. We assume that the centreline of the ribbon lies in the $\mathbf{e}_2 - \mathbf{e}_3$ plane without undergoing any twist in the deformed configuration. The centreline representation of the deformed planar ribbon is given by

$$\mathbf{x}(s, \tilde{a}, \tilde{t}) = \mathbf{r}(s) + \tilde{a}\mathbf{d}_1(s) + \tilde{t}\mathbf{d}_2(s). \quad (1)$$

Here, $\mathbf{r}(s)$ denotes the position vector of a centreline material point, $(\mathbf{d}_1(s), \mathbf{d}_2(s), \mathbf{d}_3(s))$ is the orthonormal material frame basis, and $s \in [0, l]$, $\tilde{a} \in [-\frac{a}{2}, \frac{a}{2}]$, $\tilde{t} \in [-\frac{t}{2}, \frac{t}{2}]$. The ribbon is assumed to be inextensible, uniform and obeys Kirchhoff's hypothesis, that is, normal sections to the centreline remain normal after deformation [4]. The condition of inextensibility implies $\frac{d\mathbf{r}}{ds} = \mathbf{d}_3(s)$. Also, since the ribbon does not twist, we have $\mathbf{d}_1(s) = \mathbf{e}_1$. The schematic of the centerline in the deformed configuration is shown in Fig. 3 and the coordinates of the centerline in $(\mathbf{e}_1, \mathbf{e}_2, \mathbf{e}_3)$ basis is given as follows:

$$x(s) = 0, \quad (2)$$

$$y(s) = \int_0^s \sin \theta(t) dt, \quad (3)$$

$$z(s) = \int_0^s \cos \theta(t) dt, \quad (4)$$

where s denotes arc length coordinate, $\theta(s)$ is the angle between $\mathbf{d}_3(s)$ and \mathbf{e}_3 basis vector at s .

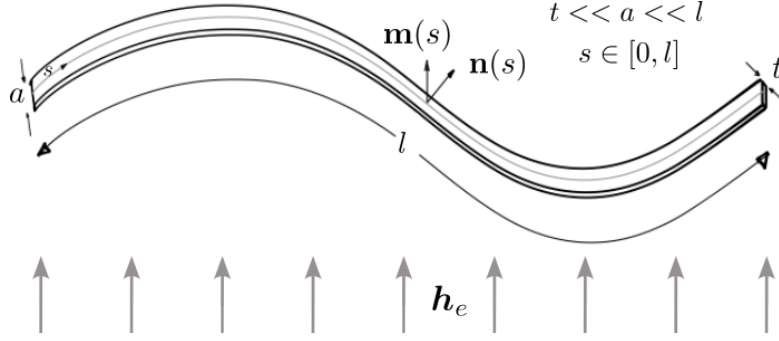


Fig. 2: Geometry of the ferromagnetic ribbon illustrating the representation of magnetisation vector $\mathbf{m}(s)$ and normal vector $\mathbf{n}(s) = \mathbf{d}_2(s)$.

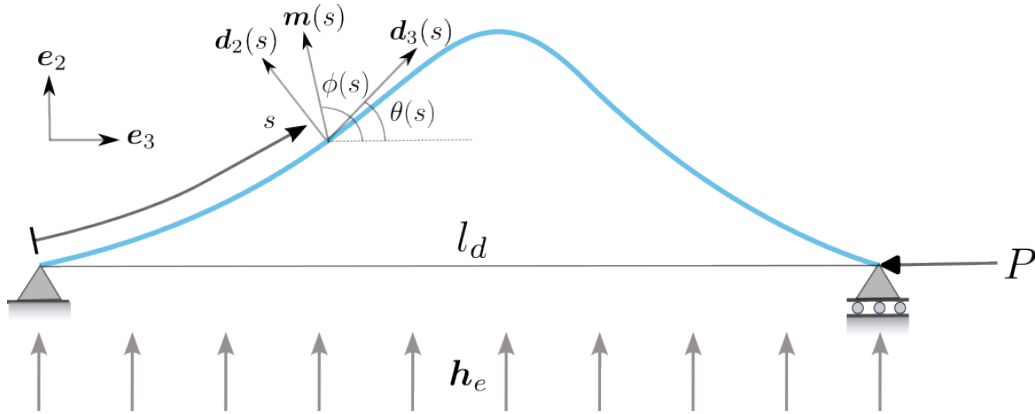


Fig. 3: Schematic setup of the ferromagnetic ribbon.

2.2 Energy formulation

The free energy functional of ferromagnetic ribbon is equal to the sum of its magnetic energy, elastic energy and the loading device energy. We will assume that the primary source of the magnetic energy arises from the demag. energy and Zeeman energy.

Given our assumption that the ribbon is made of an inextensible ferromagnetic material, the primary source of the elastic energy is the bending energy. We denote the sum of the bending energy and the loading device energy as $\mathcal{E}_{\text{elastica}}$ which is given as follows:

$$\mathcal{E}_{\text{elastica}} = \underbrace{\frac{1}{2} \int_0^l EI \kappa^2(s) ds}_{\text{Elastic (or bending) energy}} + \underbrace{P \left(1 - \int_0^l \cos \theta(s) ds \right)}_{\text{Loading energy}}, \quad (5)$$

subject to the integral constraint

$$y(l) = \int_0^l \sin \theta(s) ds = 0. \quad (6)$$

Here, $\kappa(s) = \frac{d\theta(s)}{ds}$ is the bending curvature, E is the Young's modulus, $I = \frac{at^3}{12}$ is the area moment of inertia (EI is the bending stiffness of the cross section), and P is the horizontal load.

We now proceed to write down the magnetic energy of the ribbon. We employ the theoretical framework of micromagnetics to formulate the magnetic energy associated with a ferromagnetic ribbon. Recall that the magnetisation vector: $\mathbf{m}(\mathbf{x})$, is the primary variable in the micromagnetics functional. The magnetisation vector $\mathbf{m}(\mathbf{x})$ is supported on Ω and $|\mathbf{m}(\mathbf{x})| = 1, \mathbf{x} \in \Omega$. In our analysis, Ω represents the deformed planar ferromagnetic ribbon. We now examine the various terms of the micromagnetic functional when applied to our ferromagnetic ribbon. For a detailed exposition on the micromagnetic functional, we refer the reader to [7].

The exchange energy penalizes the gradient of the magnetisation and is expressed as follows:

$$\mathcal{E}_{ex} = A \int_{\Omega} |\nabla \mathbf{m}(\mathbf{x})|^2 d\mathbf{x}, \quad (7)$$

where A is a material parameter known as the exchange constant. The exchange energy constrains the magnetisation to vary exclusively along the arc length parameter s . If the magnetisation varies across the width and thickness of the sample, the exchange energy per unit volume scales as $\mathcal{O}(\frac{A}{w^2})$ and $\mathcal{O}(\frac{A}{l^2})$, respectively. The small values of t and w , that is $t < w \ll \sqrt{A}$, prevent spatial variation in magnetisation across the width and thickness. Consequently, we assume that magnetisation only varies along the length of the ribbon, i.e., $\mathbf{m}(\mathbf{x}) = \mathbf{m}(s)$. Further, we shall assume that $l \gg \sqrt{A}$, such that $\frac{A}{l^2} \ll 1$, and hence we can ignore the exchange energy per unit volume if $\mathbf{m}(\mathbf{x}) = \mathbf{m}(s)$.

The magnetocrystalline anisotropy energy governs the favored orientations for the magnetisation vector within the ferromagnetic sample. It is quantified by the material parameter K_a , known as the anisotropy constant. In *Case 1. (soft ferromagnet)*, $K_a \ll 1$ and the magnetocrystalline anisotropy energy is very small, and the magnetisation has no preferred direction of orientation. Whereas, in *Case 2. (hard ferromagnet)*, $K_a \gg 1$ the magnetocrystalline anisotropy energy is very large and the magnetisation vector makes a fixed angle with tangent along the length of the ribbon.

We now write down the demag. energy of the planar ribbon. The demag. energy associated with planar ribbon is computed by solving Maxwell's equations of magnetostatics, namely,

$$\nabla \times \mathbf{h}_m(\mathbf{x}) = \mathbf{0}, \quad (8)$$

$$\nabla \cdot (\mathbf{h}_m(\mathbf{x}) + \mathbf{m}(\mathbf{x})) = 0. \quad (9)$$

Here, $\mathbf{m}(\mathbf{x})$ is the magnetisation vector defined on the ferromagnetic body and is equal to zero outside the body. The field induced due to the magnetisation $\mathbf{m}(\mathbf{x})$ is denoted by $\mathbf{h}_m(\mathbf{x})$. The induced magnetic field $\mathbf{h}_m(\mathbf{x})$ can be found by solving Maxwell's equations of magnetostatics.

The demag. energy is evaluated by computing the square of the L^2 -norm of $\mathbf{h}_m(\mathbf{x})$ on all of \mathbb{R}^3 , it can be conveniently calculated in terms of Fourier transform of $\mathbf{m}(\mathbf{x})$, as follows ¹

$$\mathcal{E}_{demag.} = K_d \int_{\mathbb{R}^2} |\mathbf{h}_m|^2 d\mathbf{x} = K_d \int_{\mathbb{R}^3} \frac{|\widehat{\nabla \cdot \mathbf{m}}(\boldsymbol{\xi})|^2}{|\boldsymbol{\xi}|^2} d\boldsymbol{\xi}, \quad (10)$$

where $K_d = \frac{M_s^2}{2\mu_0}$ is the magnetostatic energy constant, M_s is the saturation magnetization of the material, and μ_0 is the permeability of the free space.

We carry out the above integration in the material frame $(\mathbf{d}_1(s), \mathbf{d}_2(s), \mathbf{d}_3(s))$. In the material frame, $\mathbf{x} \mapsto \mathbf{r}(s) + \tilde{a}\mathbf{d}_1(s) + \tilde{t}\mathbf{d}_2(s)$, and $s \in [0, l]$, $\tilde{a} \in [-\frac{a}{2}, \frac{a}{2}]$, $\tilde{t} \in [-\frac{t}{2}, \frac{t}{2}]$, and $\mathbf{r}'(s) = \mathbf{d}_3(s)$. The Fourier transform of \mathbf{m} in the material frame as follows:

$$\widehat{\nabla \cdot \mathbf{m}}(\boldsymbol{\xi}) = \int (\nabla \cdot \mathbf{m}) \exp(-i2\pi \mathbf{x} \cdot \boldsymbol{\xi}) d\mathbf{x} \quad (11)$$

$$= \int \frac{1}{J} (\partial_{\tilde{a}} m_{d_1} + \partial_{\tilde{t}} + \kappa[\tilde{t}\partial_{\tilde{a}} m_{d_1} + \tilde{t}\partial_{\tilde{t}} m_{d_2} + m_{d_2}]) \exp(-i2\pi(s\xi_{d_3} + \tilde{a}\xi_{d_1} + \tilde{t}\xi_{d_2})) J ds d\tilde{a} d\tilde{t}. \quad (12)$$

¹ Details of this calculation and other computations involved in this section can be found in appendix A.

Here, J is the Jacobian involved in computing the divergence of \mathbf{m} and in the change of variables from (x_1, x_2, x_3) to $(s, \tilde{a}, \tilde{t})$. Furthermore, $m_{d_i} = \mathbf{m} \cdot \mathbf{d}_i(s)$, $\xi_{d_i} = \boldsymbol{\xi} \cdot \mathbf{d}_i(s)$.

Since the ribbon under study is narrow, we shall assume $\mathbf{m}(\mathbf{x}) = \mathbf{m}(s)$ and in the above computation, the magnetostatic or demag. energy simplifies as follows:

$$\begin{aligned} \mathcal{E}_{\text{demag.}} &= K_d \int_{\mathbb{R}^3} \frac{|\widehat{\nabla \cdot \mathbf{m}(\boldsymbol{\xi})}|^2}{|\boldsymbol{\xi}|^2} d\boldsymbol{\xi} = K_d \int_{\mathbb{R}^3} \frac{|\widehat{\nabla \cdot \mathbf{m}(\xi_{d_1}, \xi_{d_2}, \xi_{d_3})}|^2}{\xi_{d_1}^2 + \xi_{d_2}^2 + \xi_{d_3}^2} d\xi_{d_1} d\xi_{d_2} d\xi_{d_3} \\ &= K_d a t \int_{\mathbb{R}} |\widehat{m_{d_3}}(\xi_{d_2})|^2 d\xi_{d_3} + \mathcal{O}(t^2) \\ &= K_d a t \int_{s=0}^l (m_{d_2})^2 ds + \mathcal{O}(t^2) \\ &= K_d a t \int_0^l (\mathbf{m} \cdot \mathbf{d}_2)^2 ds + \mathcal{O}(t^2). \end{aligned} \quad (13)$$

The Zeeman energy of the ribbon due to external magnetic field \mathbf{h}_e is

$$\mathcal{E}_{\text{Zeeman}} = -2K_d a t \int_0^l \mathbf{h}_e \cdot \mathbf{m} ds. \quad (14)$$

In this paper, we shall only consider the leading order magnetostatic energy and hence our total magnetic energy is

$$\mathcal{E}_{\text{magnetic}} = \mathcal{E}_{\text{demag.}} + \mathcal{E}_{\text{Zeeman}} = K_d a t \int_0^l (\mathbf{m} \cdot \mathbf{d}_2)^2 ds - 2K_d a t \int_0^l \mathbf{h}_e \cdot \mathbf{m} ds. \quad (15)$$

Therefore, the total energy is the sum of $\mathcal{E}_{\text{magnetic}}$ (Eqn. (15)) and $\mathcal{E}_{\text{elastica}}$ (Eqn. (5)) and is given as follows:

$$\mathcal{E}(\theta, \mathbf{m}) = \frac{1}{2} \int_0^l EI \kappa^2(s) ds + P \left(1 - \int_0^l \cos \theta(s) ds \right) + K_d a t \int_0^l (\mathbf{m} \cdot \mathbf{d}_2)^2 ds - 2K_d a t \int_0^l \mathbf{h}_e \cdot \mathbf{m} ds. \quad (16)$$

2.3 Planar deformation of magnetoelastic ribbons

Incorporating the integral constraint (Eqn. 6), the augmented energy functional for magnetoelastic ribbon, here, ferromagnetic ribbon, is expressed as

$$\begin{aligned} \mathcal{E}(\theta, \mathbf{m}) &= \frac{1}{2} \int_0^l EI \kappa^2(s) ds + P \left(1 - \int_0^l \cos \theta(s) ds \right) + K_d a t \int_0^l (\mathbf{m} \cdot \mathbf{d}_2)^2 ds \\ &\quad - 2K_d a t \int_0^l \mathbf{h}_e \cdot \mathbf{m} ds - R \int_0^l \sin \theta(s) ds \end{aligned} \quad (17)$$

The tangent vector field $\mathbf{d}_3(s)$ (or $\mathbf{t}(s)$) is $\mathbf{d}_3(s) = (0, \sin \theta(s), \cos \theta(s))$ and so the normal vector field [20] is $\mathbf{d}_2(s) = \frac{d\mathbf{t}}{ds} / \left| \frac{d\mathbf{t}}{ds} \right| = (0, \cos \theta(s), -\sin \theta(s))$. Since $|\mathbf{m}(s)| = 1$, we can write $\mathbf{m} = (0, \sin \phi(s), \cos \phi(s))$, $\phi(s)$ is the angle between $\mathbf{m}(s)$ and \mathbf{e}_3 at s . Similarly, external magnetic field can be represented as $\mathbf{h}_e = h_e(0, \sin \psi, \cos \psi)$, where ψ is the angle between \mathbf{h}_e and \mathbf{e}_3 , and h_e is the strength of the externally applied magnetic field. Substituting

the expressions for \mathbf{m} and \mathbf{h}_e into Eqn. 17 leads to

$$\begin{aligned}\mathcal{E}(\theta, \phi) &= \frac{EI}{2} \int_0^l (\theta'(s))^2 ds + K_d at \int_0^l (-\sin \theta \cos \phi + \cos \theta \sin \phi)^2 ds - 2K_d ath_e \int_0^l (\cos \psi \cos \phi + \sin \psi \sin \phi) ds \\ &\quad - P \left(1 - \int_0^l \cos \theta(s) ds \right) - R \int_0^l \sin \theta(s) ds \\ &= \frac{EI}{2} \int_0^l (\theta'(s))^2 ds + K_d at \int_0^l \sin^2(\phi - \theta) ds - 2K_d ath_e \int_0^l \cos(\phi - \psi) ds \\ &\quad - P \left(1 - \int_0^l \cos \theta(s) ds \right) - R \int_0^l \sin \theta(s) ds.\end{aligned}\quad (18)$$

We use a non-dimensional arc length parameter defined as $\bar{s} := \frac{s}{l}$ and define $\Theta(\bar{s})$ and $\Phi(\bar{s})$ as follows:

$$\Theta(\bar{s}) = \theta(s(\bar{s})), \quad \Phi(\bar{s}) = \phi(s(\bar{s})). \quad (19)$$

The augmented energy functional is also non-dimensionalized as follows:

$$\begin{aligned}\bar{\mathcal{E}}(\Theta, \Phi) &= \frac{\mathcal{E}(\Theta, \Phi)}{EI/l} = \frac{1}{2} \int_0^1 (\Theta'(\bar{s}))^2 d\bar{s} + \bar{K}_d \int_0^1 \sin^2(\Phi(\bar{s}) - \Theta(\bar{s})) d\bar{s} - 2\bar{K}_d h_e \int_0^1 \cos(\Phi(\bar{s}) - \psi) d\bar{s} \\ &\quad - \bar{P} \left(1 - \int_0^1 \cos \Theta(\bar{s}) d\bar{s} \right) - \bar{R} \int_0^1 \sin \Theta(\bar{s}) d\bar{s},\end{aligned}\quad (20)$$

where, \bar{K}_d , \bar{P} and \bar{Q} are non-dimensional numbers defined as follows:

$$\bar{K}_d = \frac{K_d at l^2}{EI} = \frac{12K_d}{E} \left(\frac{l}{t} \right)^2, \quad \bar{P} = \frac{Pl^2}{EI} \quad \text{and} \quad \bar{R} = \frac{Rl^2}{EI}.$$

Note that \bar{K}_d is an important non-dimensional number in our analysis and represents the ratio of the demag. energy and the elastic energy of the ferromagnetic ribbon. It depends on the material properties and the aspect ratio ($\frac{l}{t}$) of the ferromagnetic ribbon. Henceforth, for simplification, we replace Θ and Φ with θ and ϕ , respectively. We will now tailor our energy functional for the two following scenarios: 1. soft ferromagnetic ribbon and 2. hard ferromagnetic ribbon.

2.4 Case 1. Soft ferromagnet.

A soft ferromagnet is a ferromagnet with very small magnetic anisotropy energy ($K_a \ll 1$), [6]. The magnetisation vector has no preferred direction of alignment within the ferromagnetic solid. Thus, the magnetisation vector rotates and aligns along the externally applied magnetic field for sufficiently large fields (Fig. 4). That is, $\mathbf{m}(\bar{s}) \parallel \mathbf{h}_e$, and as a result, the Zeeman energy is minimized and not considered in the analysis. The deformation in this case is driven by the interplay among demag. energy, bending energy, and loading device energy.

Since $\mathbf{m}(\bar{s}) \parallel \mathbf{h}_e$, we have $\mathbf{m}(\bar{s}) \cdot \mathbf{h}_e = h_e$ implying that $\phi(\bar{s}) = \psi$. Therefore, Eqn. 20 becomes

$$\bar{\mathcal{E}}(\theta, \phi) = \frac{1}{2} \int_0^1 (\theta'(\bar{s}))^2 d\bar{s} + \bar{K}_d \int_0^1 \sin^2(\phi(\bar{s}) - \theta(\bar{s})) d\bar{s} + \bar{P} \int_0^1 \cos \theta(\bar{s}) d\bar{s} - \bar{R} \int_0^1 \sin \theta(\bar{s}) d\bar{s} - \bar{P} - 2\bar{K}_d h_e. \quad (21)$$

We now proceed to derive the Euler-Lagrange equations, i.e., equilibrium equations and generic boundary conditions. Introducing first order perturbations to the unknown variables θ and ϕ as $\tilde{\theta}(\bar{s}) = \theta(\bar{s}) + \epsilon \eta(\bar{s})$, and putting it into Eqn. 21 gives

$$\begin{aligned}\bar{\mathcal{E}}(\tilde{\theta}, \psi) &= \frac{1}{2} \int_0^1 (\theta'(\bar{s}) + \epsilon \eta'(\bar{s}))^2 d\bar{s} + \bar{K}_d \int_0^1 \sin^2(\psi - \theta(\bar{s}) - \epsilon \eta(\bar{s})) d\bar{s} + \bar{P} \int_0^1 \cos(\theta(\bar{s}) + \epsilon \eta(\bar{s})) d\bar{s} \\ &\quad - \bar{R} \int_0^1 \sin(\theta(\bar{s}) + \epsilon \eta(\bar{s})) d\bar{s} - \bar{P} - 2\bar{K}_d h_e.\end{aligned}\quad (22)$$

Taking first variational of $\mathcal{E}(\tilde{\theta}, \psi)$ and equating it to zero gives us the following:

$$\left. \frac{d\bar{\mathcal{E}}(\tilde{\theta}, \psi)}{d\epsilon} \right|_{\epsilon=0} = \frac{1}{2} \int_0^1 \theta'(\bar{s}) \eta'(\bar{s}) d\bar{s} - \bar{K}_d \int_0^1 2 \sin(\psi - \theta(\bar{s})) \cos(\psi - \theta(\bar{s})) \eta(\bar{s}) d\bar{s} - \bar{P} \int_0^1 \sin(\theta(\bar{s})) \eta(\bar{s}) d\bar{s} - \bar{R} \int_0^1 \cos(\theta(\bar{s})) \eta(\bar{s}) d\bar{s} = 0. \quad (23)$$

Integrating by parts the first term on the right and then gathering terms containing $\eta(s)$ we get:

$$\theta'(\bar{s}) \eta(\bar{s}) \Big|_0^1 - \int_0^1 \left[\theta''(\bar{s}) + \bar{K}_d \sin 2(\psi - \theta(\bar{s})) + \bar{P} \sin \theta(\bar{s}) + \bar{R} \cos \theta(\bar{s}) \right] \eta(\bar{s}) d\bar{s} = 0.$$

Invoking fundamental lemma of calculus of variations, we obtain the equilibrium equations and the generic boundary conditions for the soft magnetic material as follows:

$$\begin{aligned} \theta''(\bar{s}) + \bar{K}_d \sin 2(\psi - \theta(\bar{s})) + \bar{P} \sin \theta(\bar{s}) + \bar{R} \cos \theta(\bar{s}) &= 0, \\ \theta'(\bar{s}) \eta(\bar{s}) \Big|_{\bar{s}=0} &= 0, \\ \theta'(\bar{s}) \eta(\bar{s}) \Big|_{\bar{s}=1} &= 0. \end{aligned} \quad (24)$$

We consider the case when \mathbf{h}_e is oriented along \mathbf{e}_2 -axis, and thus, $\phi(\bar{s}) = \psi = \frac{\pi}{2}$. Substituting these values of $\phi(\bar{s})$ and ψ into Eqn. 24, we obtain:

$$\theta''(\bar{s}) + \bar{K}_d \sin 2\theta(\bar{s}) + \bar{P} \sin \theta(\bar{s}) + \bar{R} \cos \theta(\bar{s}) = 0, \quad (25)$$

subject to the constraint:

$$\bar{y}(1) = \int_0^1 \sin \theta(\bar{s}) d\bar{s} = 0. \quad (26)$$

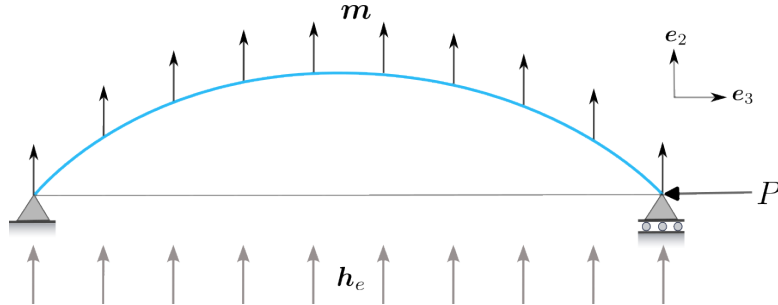


Fig. 4: Soft ferromagnetic ribbon under the influence of a transverse external magnetic field.

When $\bar{K}_d = 0$, we obtain the equilibrium equation for the classical Euler's Elastica as follows:

$$\theta''(\bar{s}) + \bar{P} \sin \theta(\bar{s}) + \bar{R} \cos \theta(\bar{s}) = 0. \quad (27)$$

We consider three canonical boundary conditions for our analysis, namely

- fixed-fixed: $\theta(\bar{s} = 0) = 0, \theta(\bar{s} = 1) = 0,$
- pinned-pinned: $\theta'(\bar{s} = 0) = 0, \theta'(\bar{s} = 1) = 0,$
- fixed-free: $\theta(\bar{s} = 0) = 0, \theta'(\bar{s} = 1) = 0.$

Note that the constraint (Eqn. (26)) does not apply for fixed-free condition.

2.5 Case 2. Hard ferromagnet.

A hard ferromagnet is a ferromagnet with very large magnetic anisotropy energy ($K_a \gg 1$). The magnetic anisotropy energy is minimised when the magnetization vector aligns along a preferred direction within the ferromagnetic solid. Thus, in a hard ferromagnetic ribbon, magnetization vector ($\mathbf{m}(\bar{s})$) makes a constant angle with the tangent ($\mathbf{d}_3(\bar{s})$) along the entire length of the curve. $\mathbf{m}(\bar{s})$ varies spatially along the length of the curve to maintain a constant angle with the tangent of the curve as the ribbon deforms. We will consider that $\mathbf{m}(\bar{s})$ is either aligned along the normal ($\mathbf{m}(\bar{s}) \perp \mathbf{d}_3(\bar{s})$) or that it is aligned along the tangent ($\mathbf{m}(\bar{s}) \parallel \mathbf{d}_3(\bar{s})$) of the curve $\mathbf{r}(\bar{s})$, see Figs. 5a and 5b. Note that, in this case $(\mathbf{m} \cdot \mathbf{n})^2$ is constant and hence the demag. energy does not participate in energy minimization. The deformation in this case is driven by the interplay among Zeeman energy, bending energy, and loading device energy. We study the deformation of a hard ferromagnetic ribbon with the external magnetic field aligned in both the transverse and axial directions.

In this case, the magnetization direction reorients as a result of induced deformation due to the presence of \mathbf{h}_e . The magnetization vector field for the deformed configuration is given by

$$\mathbf{m}(\bar{s}) = (0, \sin \phi(\bar{s}), \cos \phi(\bar{s})). \quad (28)$$

Substituting this expression of $\mathbf{m}(\bar{s})$ in Eqn. 20 leads us to

$$\begin{aligned} \bar{\mathcal{E}}(\theta, \psi) = & \frac{1}{2} \int_0^1 (\theta'(\bar{s}))^2 d\bar{s} + \bar{K}_d \int_0^1 \sin^2(\phi(\bar{s}) - \theta(\bar{s})) d\bar{s} - 2\bar{K}_d h_e \int_0^1 \cos(\phi(\bar{s}) - \psi) d\bar{s} \\ & + \bar{P} \int_0^1 \cos \theta(\bar{s}) d\bar{s} - \bar{Q} \int_0^1 \sin \theta(\bar{s}) d\bar{s} - \bar{P} \end{aligned} \quad (29)$$

where \bar{Q} is a Lagrange multiplier introduced to distinguish from \bar{R} . Recall \bar{R} is the vertical reaction for the Euler's Elastica (see Eqn. 27). Following similar steps as in soft magnetization scenario, we arrive at the following Euler-Lagrange equations for hard magnetization case as

$$\begin{aligned} \theta''(\bar{s}) + \bar{P} \sin \theta(\bar{s}) - 2\bar{K}_d h_e \sin(\phi(\bar{s}) - \psi) + \bar{Q} \cos \theta(\bar{s}) &= 0, \\ \theta'(\bar{s}) \eta(\bar{s})|_{\bar{s}=0} &= 0, \\ \theta'(\bar{s}) \eta(\bar{s})|_{\bar{s}=1} &= 0. \end{aligned} \quad (30)$$

We consider tangential and normal uniform magnetization distributions such that $\phi(\bar{s}) = \theta(\bar{s}), \theta(\bar{s}) + \frac{\pi}{2}$ respectively. We expose the hard ferromagnetic ribbon to axial and transverse external magnetic fields, i.e., $\psi = 0, \frac{\pi}{2}$. The corresponding equilibrium equations are enumerated as

$$\begin{aligned} \mathbf{h}_e = \mathbf{e}_3 : \mathbf{m}(\bar{s}) = \mathbf{t}(\bar{s}) : \theta''(\bar{s}) + (\bar{P} - 2\bar{K}_d h_e) \sin \theta(\bar{s}) + \bar{Q} \cos \theta(\bar{s}) &= 0, \\ \mathbf{m}(\bar{s}) = \mathbf{n}(\bar{s}) : \theta''(\bar{s}) + \bar{P} \sin \theta(\bar{s}) + (\bar{Q} - 2\bar{K}_d h_e) \cos \theta(\bar{s}) &= 0, \\ \mathbf{h}_e = \mathbf{e}_2 : \mathbf{m}(\bar{s}) = \mathbf{t}(\bar{s}) : \theta''(\bar{s}) + \bar{P} \sin \theta(\bar{s}) + (\bar{Q} + 2\bar{K}_d h_e) \cos \theta(\bar{s}) &= 0, \\ \mathbf{m}(\bar{s}) = \mathbf{n}(\bar{s}) : \theta''(\bar{s}) + (\bar{P} - 2\bar{K}_d h_e) \sin \theta(\bar{s}) + \bar{Q} \cos \theta(\bar{s}) &= 0. \end{aligned} \quad (31)$$

3 Path continuation methodology

We determine numerical solutions to the equilibrium equations as the loading parameter \bar{P} is quasi-statically varied for various loading scenarios. We utilize a continuation method called pseudo arc length-based technique as discussed in [19] to determine the deformed configurations. The technique constrains the incremental deformation measure and increment in load parameters (P, R) via a hyperspheric constraint.

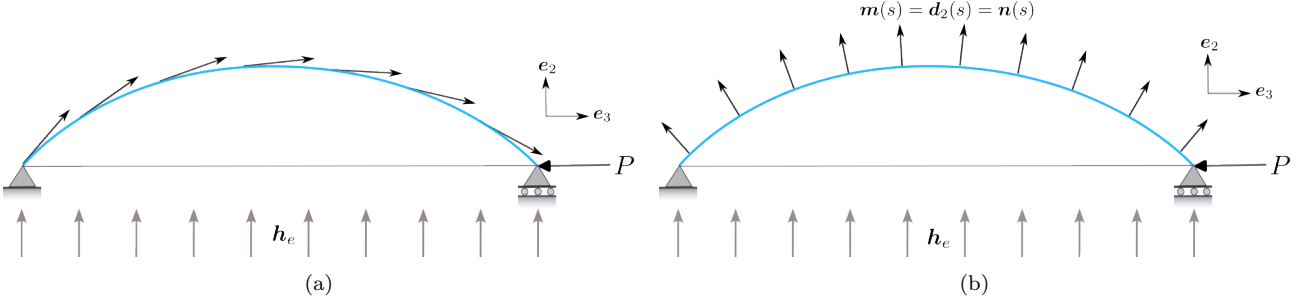


Fig. 5: Magnetically hard ferromagnetic ribbon under the influence of an external magnetic field: (a) Magnetization along the tangential direction, (b) Magnetization along the normal direction.

3.1 Discretization of equilibrium equations

We discretize Eqn. (24) for fixed-fixed boundary conditions. We discretize the domain into $N + 1$ nodal points as $\bar{s}_i = ih; i = 0, 1, \dots, N + 1$ where $h = \frac{1}{N+1}$. We utilize second-order accurate central difference scheme to approximate the second-order derivative in Eqn. (24). The discrete system of equations along with the boundary conditions is

$$\frac{\theta_{i-1} - 2\theta_i + \theta_{i+1}}{h^2} + \bar{P} \sin \theta_i + \bar{K}_d \sin 2\theta_i + \bar{R} \cos \theta_i = 0; \quad i = 1, 2, \dots, N, \quad (32)$$

$$\theta_0 = 0, \theta_{N+1} = 0,$$

where θ_i denotes the numerical counterpart of $\theta(\bar{s} = \bar{s}_i)$. In matrix-vector form, the discretized system can be written for all three cases (for fixed-free case where $\bar{R} = 0$) as

$$\mathbf{K}\boldsymbol{\theta} + \bar{P} \sin \boldsymbol{\theta} + \bar{K}_d \sin 2\boldsymbol{\theta} + \bar{R} \cos \boldsymbol{\theta} = \mathbf{0} \quad (\text{see appendix B for } \mathbf{K} \text{ and } \boldsymbol{\theta}). \quad (33)$$

Incorporating the discretized form of integral constraint (Eqn. (26)) results in the combined nonlinear system of equations (for fixed-fixed and pinned-pinned conditions)

$$\begin{pmatrix} \mathbf{K}\boldsymbol{\theta} + \bar{P} \sin \boldsymbol{\theta} + \bar{K}_d \sin 2\boldsymbol{\theta} + \bar{R} \cos \boldsymbol{\theta} \\ \sin \theta_1 + \dots + \sin \theta_N \end{pmatrix} = \begin{pmatrix} \mathbf{0} \\ 0 \end{pmatrix}, \quad (34)$$

or, $\mathbf{f}(\boldsymbol{\theta}, \bar{R}, \bar{P}) = \mathbf{0}$.

3.2 Pseudo arc length-based continuation method

We proceed to devise a strategy to solve the nonlinear system of equations (Eqn. (34)) using an arc length-based continuation method. Let us describe k -th configuration of the planar-deforming ferromagnetic ribbon as $(\boldsymbol{\theta}_k, \bar{R}_k, \bar{P}_k)$ where k denotes the configuration index. The algorithm works in two steps: prediction step and correction step.

Prediction step : We expand the equilibrium equation (Eqn. (34)) at $(k + 1)$ -th index in terms of Taylor series expansion about k as

$$\underbrace{\mathbf{f}(\boldsymbol{\theta}_{k+1}, \bar{R}_{k+1}, \bar{P}_{k+1})}_{=0} = \underbrace{\mathbf{f}(\boldsymbol{\theta}_k, \bar{R}_k, \bar{P}_k)}_{=0} + \frac{\partial \mathbf{f}}{\partial \boldsymbol{\theta}} \Big|_k \Delta \boldsymbol{\theta}_k + \frac{\partial \mathbf{f}}{\partial \bar{R}} \Big|_k \Delta \bar{R}_k + \frac{\partial \mathbf{f}}{\partial \bar{P}} \Big|_k \Delta \bar{P}_k + \underbrace{\mathcal{O}(\Delta \boldsymbol{\theta}_k^2, \Delta \bar{R}_k^2, \Delta \bar{P}_k^2)}_{\text{ignore}}, \quad (35)$$

$$\implies \frac{\partial \mathbf{f}}{\partial \boldsymbol{\theta}} \Big|_k \Delta \boldsymbol{\theta}_k + \frac{\partial \mathbf{f}}{\partial \bar{R}} \Big|_k \Delta \bar{R}_k + \frac{\partial \mathbf{f}}{\partial \bar{P}} \Big|_k \Delta \bar{P}_k = \mathbf{0}. \quad (36)$$

We define a tangent vector as

$$\mathbf{e}_k = \begin{pmatrix} \Delta\boldsymbol{\theta}_k \\ \Delta\bar{R}_k \\ \Delta\bar{P}_k \end{pmatrix}, \quad (37)$$

whose norm squared is

$$\|\mathbf{e}_k\|^2 = (\Delta\boldsymbol{\theta}_k)^T(\Delta\boldsymbol{\theta}_k) + (\Delta\bar{R}_k)^2 + (\Delta\bar{P}_k)^2. \quad (38)$$

We make the following substitution

$$\Delta\bar{P}_k = a_k, \quad \Delta\bar{R}_k = a_k\Delta r_k, \quad \Delta\boldsymbol{\theta}_k = a_k\Delta\boldsymbol{\phi}_k. \quad (39)$$

Setting the norm of \mathbf{e}_k to unity, we obtain the expression for a_k

$$a_k^2(\Delta\boldsymbol{\phi}_k)^T(\Delta\boldsymbol{\phi}_k) + a_k^2(\Delta r_k)^2 + a_k^2 = 1, \quad (40)$$

$$\implies a_k = \pm \frac{1}{\sqrt{(\Delta\boldsymbol{\phi}_k)^T(\Delta\boldsymbol{\phi}_k) + (\Delta r_k)^2 + 1}}. \quad (41)$$

The sign of a_k is chosen positive if $\mathbf{e}_{k-1}^T \mathbf{e}_k > 0$ or else a_k is taken to be negative. Substituting the expressions for $\Delta\boldsymbol{\theta}_k, \Delta\bar{R}_k$ and $\Delta\bar{P}_k$ in Eqn. (36), we have

$$\left. \frac{\partial \mathbf{f}}{\partial \boldsymbol{\theta}} \right|_k a_k \Delta\boldsymbol{\phi}_k + \left. \frac{\partial \mathbf{f}}{\partial \bar{R}} \right|_k a_k \Delta r_k + \left. \frac{\partial \mathbf{f}}{\partial \bar{P}} \right|_k a_k = \mathbf{0}, \quad (42)$$

$$\implies \begin{bmatrix} \left. \frac{\partial \mathbf{f}}{\partial \boldsymbol{\theta}} \right|_k & \left. \frac{\partial \mathbf{f}}{\partial \bar{R}} \right|_k \end{bmatrix} \begin{pmatrix} \Delta\boldsymbol{\phi}_k \\ \Delta r_k \end{pmatrix} = - \left. \frac{\partial \mathbf{f}}{\partial \bar{P}} \right|_k. \quad (43)$$

We use Eqn. (43) to solve for $\Delta\boldsymbol{\phi}_k, \Delta r_k$ and then compute a_k (Eqn. (41)) and \mathbf{e}_k (Eqn. (37)). We now construct the initial guess for $(k+1)$ -configuration as

$$\begin{pmatrix} \boldsymbol{\theta}_{k+1}^{(0)} \\ \bar{R}_{k+1}^{(0)} \\ \bar{P}_{k+1}^{(0)} \end{pmatrix} = \begin{pmatrix} \boldsymbol{\theta}_k \\ \bar{R}_k \\ \bar{P}_k \end{pmatrix} + \Delta s \cdot \mathbf{e}_k, \quad (44)$$

where Δs is the arc length step size. Δs is small enough to capture the bifurcation along the equilibrium path.

Correction step : We subject the predicted initial guess (Eqn. (44)) of $(k+1)$ -configuration to a sequence of corrective iterations using the widely-used Newton-Raphson technique. Denoting $(k+1)$ -configuration by $(\boldsymbol{\theta}_{k+1}, \bar{R}_{k+1}, \bar{P}_{k+1})$, we obtain the following Taylor series expansion about l -iteration level

$$\underbrace{\mathbf{f}(\boldsymbol{\theta}_{k+1}, \bar{R}_{k+1}, \bar{P}_{k+1})}_{=0} \approx \mathbf{f}(\boldsymbol{\theta}_{k+1}^{(l)}, \bar{R}_{k+1}^{(l)}, \bar{P}_{k+1}^{(l)}) + \left. \frac{\partial \mathbf{f}}{\partial \boldsymbol{\theta}} \right|_{k+1}^{(l)} \Delta\boldsymbol{\theta}_{k+1}^{(l+1)} + \left. \frac{\partial \mathbf{f}}{\partial \bar{R}} \right|_{k+1}^{(l)} \Delta\bar{R}_{k+1}^{(l+1)} + \left. \frac{\partial \mathbf{f}}{\partial \bar{P}} \right|_{k+1}^{(l)} \Delta\bar{P}_{k+1}^{(l+1)}, \quad (45)$$

$$\implies \left. \frac{\partial \mathbf{f}}{\partial \boldsymbol{\theta}} \right|_{k+1}^{(l)} \Delta\boldsymbol{\theta}_{k+1}^{(l+1)} + \left. \frac{\partial \mathbf{f}}{\partial \bar{R}} \right|_{k+1}^{(l)} \Delta\bar{R}_{k+1}^{(l+1)} + \left. \frac{\partial \mathbf{f}}{\partial \bar{P}} \right|_{k+1}^{(l)} \Delta\bar{P}_{k+1}^{(l+1)} = -\mathbf{f}(\boldsymbol{\theta}_{k+1}^{(l)}, \bar{R}_{k+1}^{(l)}, \bar{P}_{k+1}^{(l)}). \quad (46)$$

We enforce the orthogonality constraint on tangent vector at every iteration level l , which is

$$\mathbf{e}_k^T \mathbf{e}_{k+1}^{(l+1)} = 0, \quad (47)$$

$$\implies (\Delta\boldsymbol{\theta}_k)^T(\Delta\boldsymbol{\theta}_{k+1}^{(l+1)}) + (\Delta\bar{R}_k)(\Delta\bar{R}_{k+1}^{(l+1)}) + (\Delta\bar{P}_k)(\Delta\bar{P}_{k+1}^{(l+1)}) = 0. \quad (48)$$

Combining Eqns. (46) and (48) to construct the following iterative scheme

$$\begin{bmatrix} \frac{\partial \mathbf{f}}{\partial \boldsymbol{\theta}} \Big|_{k+1}^{(l)} & \frac{\partial \mathbf{f}}{\partial \bar{R}} \Big|_{k+1}^{(l)} & \frac{\partial \mathbf{f}}{\partial \bar{P}} \Big|_{k+1}^{(l)} \\ (\Delta \boldsymbol{\theta}_k)^T & \Delta \bar{R}_k & \Delta \bar{P}_k \end{bmatrix} \begin{pmatrix} \Delta \boldsymbol{\theta}_{k+1}^{(l+1)} \\ \Delta \bar{R}_{k+1}^{(l+1)} \\ \Delta \bar{P}_{k+1}^{(l+1)} \end{pmatrix} = \begin{pmatrix} -\mathbf{f}(\boldsymbol{\theta}_{k+1}^{(l)}, \bar{R}_{k+1}^{(l)}, \bar{P}_{k+1}^{(l)}) \\ 0 \end{pmatrix}. \quad (49)$$

We solve the matrix equation (Eqn. (49)) and then carry out the update procedure as

$$\begin{pmatrix} \boldsymbol{\theta}_{k+1}^{(l+1)} \\ \bar{R}_{k+1}^{(l+1)} \\ \bar{P}_{k+1}^{(l+1)} \end{pmatrix} = \begin{pmatrix} \boldsymbol{\theta}_{k+1}^{(l)} \\ \bar{R}_{k+1}^{(l)} \\ \bar{P}_{k+1}^{(l)} \end{pmatrix} + \begin{pmatrix} \Delta \boldsymbol{\theta}_{k+1}^{(l+1)} \\ \Delta \bar{R}_{k+1}^{(l+1)} \\ \Delta \bar{P}_{k+1}^{(l+1)} \end{pmatrix}. \quad (50)$$

The correction steps ($l = 1, 2, \dots$) are performed till the increments meet a prescribed tolerance. We then increment the configuration index ($k \leftarrow k + 1$) and repeat the prediction and correction steps until \bar{P}_{\max} is reached. The adopted continuation procedure is illustrated in Fig. 6.

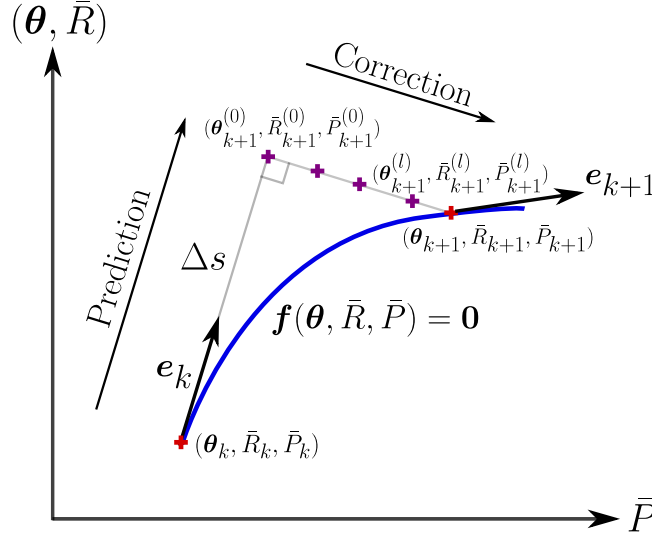


Fig. 6: Schematic of pseudo arc length-based continuation procedure showing equilibrium curve in blue.

4 Bifurcation analysis of equilibrium configuration

We now determine whether a given deformed equilibrium configuration is stable with respect to infinitesimal perturbations. Stable perturbations are physically realizable. This requires evaluation of the second variational derivative of the energy functional at the critical points. The critical points are the solutions to the Euler-Lagrange equations.

We now determine the second variational derivative of the functional, $\delta^2 \bar{\mathcal{E}}(\boldsymbol{\theta})$ for the soft magnetization ribbon when \mathbf{h}_e is applied along \mathbf{e}_2 -axis such that $\mathbf{m}(\bar{s}) = \mathbf{e}_2$. Introducing first order perturbation in the assumed extremum $\boldsymbol{\theta}$ as $\hat{\boldsymbol{\theta}}(\bar{s}) = \boldsymbol{\theta}(\bar{s}) + \epsilon \boldsymbol{\eta}(\bar{s})$ where $\boldsymbol{\eta}(\bar{s})$ is a kinematically admissible planar variation and ϵ is a small

parameter, and substituting it into Eqn. (20)

$$\begin{aligned} \bar{\mathcal{E}}(\theta + \epsilon\eta) = \frac{1}{2} \int_0^1 (\theta' + \epsilon\eta')^2 d\bar{s} + \bar{K}_d \int_0^1 \cos^2(\theta + \epsilon\eta) \theta d\bar{s} + \bar{P} \int_0^1 \cos(\theta + \epsilon\eta) d\bar{s} \\ - \bar{R} \int_0^1 \sin(\theta + \epsilon\eta) d\bar{s} + \text{constant}. \end{aligned} \quad (51)$$

Simplifying the above expansion and taking into account the boundary conditions, we have

$$\delta^2 \bar{\mathcal{E}}(\theta) = \left. \frac{d^2 \bar{\mathcal{E}}(\theta + \epsilon\eta)}{d\epsilon^2} \right|_{\epsilon=0} = - \int_0^1 [\eta'' + 2\bar{K}_d \cos 2\theta\eta + \bar{P} \cos \theta\eta - \bar{R} \sin \theta\eta] \eta d\bar{s}, \quad (52)$$

for all kinematically admissible functions $\eta(\bar{s})$. The stability criterion states that

$$\delta^2 \bar{\mathcal{E}}(\theta) \begin{cases} > 0 & \text{stable,} \\ < 0 & \text{unstable.} \end{cases} \quad (53)$$

Further, we also introduce the first variation of the integral constraint $\int_0^1 \sin \theta(\bar{s}) d\bar{s} = 0$ given as:

$$\int_0^1 \cos \theta(\bar{s}) \eta(\bar{s}) d\bar{s} = 0. \quad (54)$$

The detailed bifurcation analysis technique is presented in Appendix C.

4.1 Construction of Sturm-Liouville problem

Following [16,4], we construct an equivalent Sturm-Liouville problem for the second variation $\delta^2 \bar{\mathcal{E}}(\theta)$ as follows:

$$\phi_n''(\bar{s}) + \lambda_n (2\bar{K}_d \cos 2\theta + \bar{P} \cos \theta - \bar{R} \sin \theta) \phi_n(\bar{s}) = C_{R_n} \cos \theta(\bar{s}), \quad (55)$$

where λ_n are the eigenvalues, ϕ_n the corresponding eigenmodes of Eqn. (55) and $L(\bar{s}) = (2\bar{K}_d \cos 2\theta + \bar{P} \cos \theta - \bar{R} \sin \theta)$ denotes the weight function. C_{R_n} is a Lagrange parameter introduced to enforce the isoperimetric constraint (Eqn. (54)). The conditions on $\phi_n(\bar{s})$ are

- fixed-fixed case: $\phi_n(0) = \phi_n(1) = 0$ and $\int_0^1 \cos \theta(\bar{s}) \phi_n(\bar{s}) d\bar{s} = 0$,
- pinned-pinned case: $\phi_n'(0) = \phi_n'(1) = 0$ and $\int_0^1 \cos \theta(\bar{s}) \phi_n(\bar{s}) d\bar{s} = 0$,
- fixed-free case: $\phi_n(0) = \phi_n'(1) = 0$.

We obtain the following conditions for two arbitrary eigenmodes $\phi_m(\bar{s})$ and $\phi_n(\bar{s})$ of the Sturm-Liouville problem (Eqn. (55))

$$\lambda_n \int_0^1 L(\bar{s}) \phi_n^2 d\bar{s} = \int_0^1 \phi_n'^2 d\bar{s}, \quad (56)$$

and the orthogonality condition

$$\int_0^1 L(\bar{s}) \phi_n \phi_m d\bar{s} = 0. \quad (57)$$

The details of the above calculation can be found in appendix C.

Spectral decomposition : Let us use $\phi_n(\bar{s})$ alongwith the weight function $L(\bar{s})$ to construct a Fourier series representation (converging in the mean) to the square-integrable function $\eta(\bar{s})$,

$$\eta(\bar{s}) = \sum_{n=1}^{\infty} c_n \phi_n(\bar{s}), \quad c_n \text{ are Fourier coefficients.} \quad (58)$$

Substituting the above representation in Eqn. (52) and invoking the conditions (Eqns. (56) and (57)), we obtain the stability criterion:

$$\delta^2 \bar{\mathcal{E}}(\theta) = \sum_{n=1}^{\infty} c_n^2 \left(1 - \frac{1}{\lambda_n}\right) \int_0^1 (\phi'_n(\bar{s}))^2 d\bar{s} \quad \begin{cases} > 0 \text{ if } \lambda_n \notin [0, 1] & \text{stable,} \\ < 0 \text{ if } \lambda_n \in [0, 1] & \text{unstable.} \end{cases} \quad (59)$$

4.1.1 Numerical bifurcation analysis

We describe the numerical procedure for the fixed-fixed case, which can be easily adapted to pinned-pinned and fixed-free cases. Given, Eqn. (55) as

$$\phi_m''(\bar{s}) + \lambda_m L_m(\bar{s}) \phi_m(\bar{s}) = C_{R_m} N(\bar{s}), \quad (60)$$

where, the coefficient functions are

$$L_m(\bar{s}) = 2\bar{K}_d \cos 2\theta(\bar{s}) + \bar{P} \cos \theta(\bar{s}) - \bar{R} \sin \theta(\bar{s}), \quad N(\bar{s}) = \cos \theta(\bar{s}). \quad (61)$$

Eqn. (60) is also subjected to the boundary conditions $\phi_m(0) = 0, \phi_m(1) = 0$ and the additional constraint

$$\int_0^1 \phi_m(\bar{s}) N(\bar{s}) d\bar{s} = 0. \quad (62)$$

Numerical procedure to compute eigenvalues λ_m : Partition the interval $\bar{s} \in [0, 1]$ segments of equal length $h = \frac{1}{n+1}$ such that the starting points of the segments can be denoted by $\bar{s}_{i-1} = (i-1)h; i = 1, 2, \dots, n+1$. For i -th segment, the functions $L(\bar{s})$ and $N(\bar{s})$ are approximated by averaging their corresponding values at nodal indices i and $i+1$ resulting in L_i and N_i respectively. Substituting these averaged quantities, Eqn. (60) becomes

$$\phi_m''(\bar{s}) + \lambda_m L_i \phi_m(\bar{s}) = C_{R_m} N_i, \quad (63)$$

which is an ordinary differential equation (ODE) with constant coefficients. The solution to this ODE is

$$\phi_m(\bar{s}) = A_{1i} F_{1i}(\bar{s} - \bar{s}_{i-1}) + A_{2i} F_{2i}(\bar{s} - \bar{s}_{i-1}) + C_{R_m} \frac{N_i}{\lambda_m L_i}, \quad (64)$$

where A_{1i} and A_{2i} are constants, and the functions F_{1i} and F_{2i} are defined as

1. for $\lambda_m L_i > 0$ as $F_{1i}(\bar{s} - \bar{s}_{i-1}) = \cos a_i(\bar{s} - \bar{s}_{i-1}), \quad F_{2i}(\bar{s} - \bar{s}_{i-1}) = \sin a_i(\bar{s} - \bar{s}_{i-1}),$
2. for $\lambda_m L_i < 0$ as $F_{1i}(\bar{s} - \bar{s}_{i-1}) = \cosh a_i(\bar{s} - \bar{s}_{i-1}), \quad F_{2i}(\bar{s} - \bar{s}_{i-1}) = \sin a_i(\bar{s} - \bar{s}_{i-1})$ with $a_i = \sqrt{|\lambda L_i|}$.

The constants A_{1i} and A_{2i} can be obtained from the matching conditions

$$\phi_m(\bar{s}_{i-1}) = \phi_{m,i-1}, \quad \phi'_m(\bar{s}_{i-1}) = \phi'_{m,i-1} \quad (65)$$

as

$$A_{1i} = \phi_{m,i-1} - C_{R_m} \frac{N_i}{\lambda_m L_i}, \quad A_{2i} = \frac{\phi'_{m,i-1}}{a_i}. \quad (66)$$

The quantity $\phi_m(\bar{s}_i) = \phi_{m,i}$ at the right end of the segment is computed alongwith its derivative as

$$\begin{aligned}\phi_{m,i} &= \phi_{m,i-1}F_{1i}(h) + \frac{\phi'_{m,i-1}}{a_i}F_{2i}(h) + C_{R_m}N_i \frac{[1 - F_{1i}(h)]}{\lambda_m L_i}, \\ \phi'_{m,i} &= \phi_{m,i-1}F'_{1i}(h) + \frac{\phi'_{m,i-1}}{a_i}F'_{2i}(h) - C_{R_m}N_i \frac{F'_{1i}(h)}{\lambda_m L_i}.\end{aligned}\quad (67)$$

The general solution of Eqn. (63) can be constructed by using Eqns. (67), and the continuity requirement of ϕ_m and ϕ'_m at the extremities of every integration segment. Since Eqn. (60) is linear, its general solution can be written as a combination of three particular solutions

$$\phi_m(\bar{s}) = c_1\psi_1(\bar{s}) + c_2\psi_2(\bar{s}) + C_{R_m}\psi_3(\bar{s}), \quad (68)$$

where c_1 and c_2 are constants. We use the following initial data

$$\begin{aligned}\psi_1(0) &= 1, & \psi'_1(0) &= 0, & C_{R_m} &= 0, \\ \psi_2(0) &= 0, & \psi'_2(0) &= 1, & C_{R_m} &= 0, \\ \psi_3(0) &= 0, & \psi'_3(0) &= 0, & C_{R_m} &= 1.\end{aligned}\quad (69)$$

The functions $\psi_i(\bar{s}), i = 1, 2, 3$ can be constructed separately using the recurrence relations Eqn. (67). Using boundary conditions, we have

$$\begin{aligned}\phi_m(0) = 0 &\implies c_1 = 0, \\ \phi_m(1) = 0 &\implies c_2\psi_2(1) + C_{R_m}\psi_3(1) = 0.\end{aligned}\quad (70)$$

Substituting Eqn. (68) in Eqn. (62), the constraint can be rewritten as

$$c_2 \int_0^1 \psi_2(\bar{s})N(\bar{s})d\bar{s} + C_{R_m} \int_0^1 \psi_3(\bar{s})N(\bar{s})d\bar{s} = 0. \quad (71)$$

We construct the following homogeneous system of equations

$$\begin{bmatrix} \psi_2(1) & \psi_3(1) \\ \int_0^1 \psi_2(\bar{s})N(\bar{s})d\bar{s} & \int_0^1 \psi_3(\bar{s})N(\bar{s})d\bar{s} \end{bmatrix} \begin{pmatrix} c_2 \\ C_{R_m} \end{pmatrix} = \begin{pmatrix} 0 \\ 0 \end{pmatrix}. \quad (72)$$

For non-trivial solution to the above equation, the determinant,

$$\Delta = \psi_2(1) \int_0^1 \psi_3(\bar{s})N(\bar{s})d\bar{s} - \psi_3(1) \int_0^1 \psi_2(\bar{s})N(\bar{s})d\bar{s} \quad (73)$$

must be zero. The integrals are evaluated numerically.

We vary the value of λ_m from 0 to 1 and monitor how Δ changes

- If at least one value of $\lambda_m \in [0, 1]$ exists resulting in $\Delta = 0$, then the non-trivial solution of Eqn. (68) exists which also satisfies the boundary conditions. The corresponding equilibrium configuration is unstable.
- If no $\lambda_m \in [0, 1]$ results in $\Delta = 0$, it implies that there exists a trivial solution of Eqn. (68). The corresponding equilibrium configuration is therefore stable.

5 Results and Discussion

In this section, we begin with the validation of our numerical framework by comparing our results with the well-studied Euler's Elastica from existing literature [4]. We consider three canonical boundary conditions, namely, fixed-fixed, pinned-pinned, and fixed-free. Our results are presented as load-displacement curves, also known as equilibrium curves, which have been determined using the continuation algorithm described in Section 3. We use the well-known mathematical analysis tool, AUTO-07p, to validate numerical results. We then explore solutions for both soft and hard ferromagnetic ribbons under different loading scenarios. We have summarised all the cases considered in Table 1. The width of the ferromagnetic ribbon is assumed to be very small, allowing it to deform into self-intersecting loops while remaining planar.

Sections	5.1	5.2	5.3			
Description	Euler's Elastica	Case 1 Soft ferromagnet	Case 2: Hard ferromagnet			
		Transverse \mathbf{h}_e	Transverse \mathbf{h}_e		Axial \mathbf{h}_e	
			$m = t$	$m = n$	$m = t$	$m = n$
Figures	Fixed-Free (7) Fixed-Fixed (8) Pinned-Pinned (9)	(10) (11) (12)	(13) (14) (15)	(7) but different \bar{R} (8) ,, (9) ,,	(7) but different \bar{R} (8) ,, (9) ,,	(13) (14) (15)

Table 1: Various considered cases in the study.

5.1 Euler's Elastica

Fig. 7a shows the stability diagram for the first three nonlinear modes when the Elastica is fixed at one end while the other end remains free. We plot the horizontal displacement of the end-point, $u_3(\bar{s} = 1) = \int_0^1 \cos \theta(\bar{s}) d\bar{s}$, against loading parameter \bar{P} . Note that $\bar{P} > 0$ corresponds to compressive loads and $\bar{P} < 0$ corresponds to tensile loads. The solid curves denote stable deformations while the dotted lines represent unstable deformations.

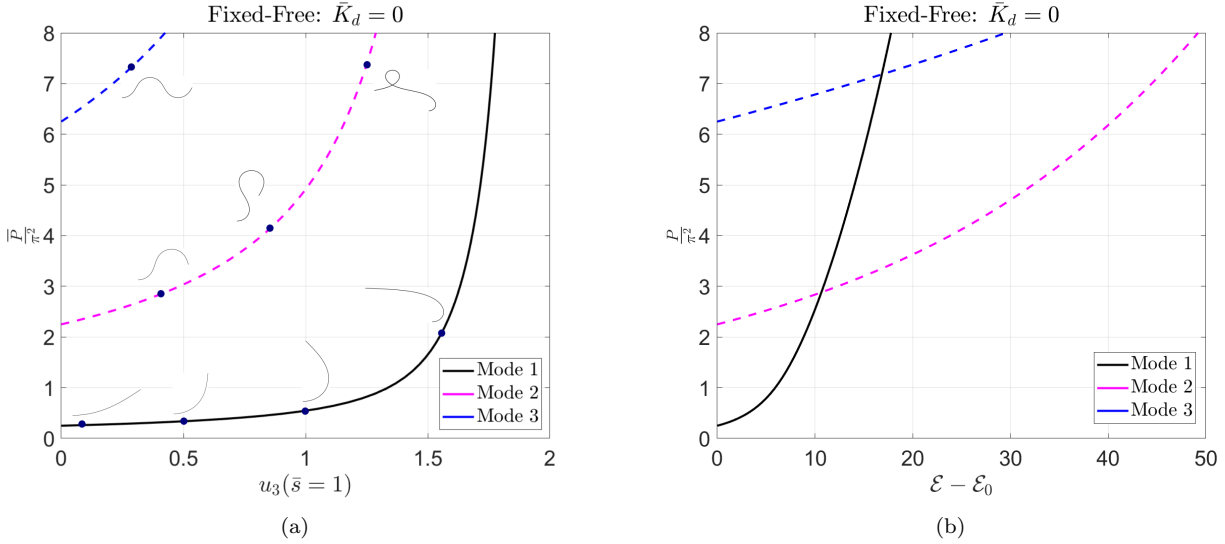


Fig. 7: Euler's Elastica: (a) Stability diagram, note that the first critical load is compressive, that is, $\bar{P}_1 = +\frac{\pi^2}{4}$. (b) Total energy curve for fixed-free configuration; $\mathcal{E}_0 = 0$.

We observe that only the first nonlinear mode is stable. The stability diagram for the fixed-fixed scenario is shown in Fig. 8a. We observe that the Elastica undergoes primary bifurcation along the first nonlinear mode initiating at the first critical \bar{P} (obtained from linearized buckling analysis). The bifurcation at first critical \bar{P} is continuous, as seen in Fig. 8b. As \bar{P} is increased beyond the first critical load, the two ends of the ribbon meet. Thereafter, it undergoes snap-through (secondary) bifurcation at $\bar{P} = 10\pi^2$ to the mode-2 branch. At the secondary bifurcation, the total energy of mode-1 becomes larger than that of mode-2, see Fig. 8. The ribbon continues to deform on the second mode for $\bar{P} > 10\pi^2$. If \bar{P} is quasi-statically reduced along the mode-2 branch, the nature of buckling load gradually switches from compressive to tensile until it snap backs to the pre-buckled (reference) tensile configuration at $\bar{P} = -6\pi^2$. The stability diagram corresponding to pinned-pinned case (Fig. 9)

shows that only mode-1 is the stable mode beyond the first critical load and it stays so till the end-points meet, after which the ribbon snaps to the pre-buckled (reference) configuration [16].

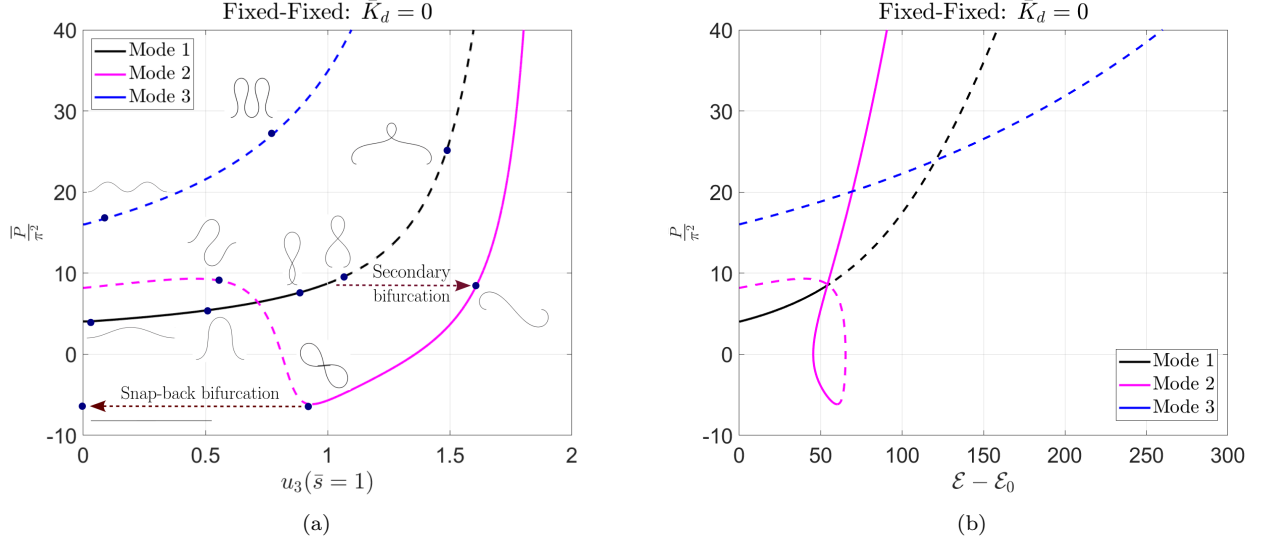


Fig. 8: Euler's Elastica: (a) Stability diagram (b) Total energy curve for fixed-fixed configuration; $\mathcal{E}_0 = 0$.

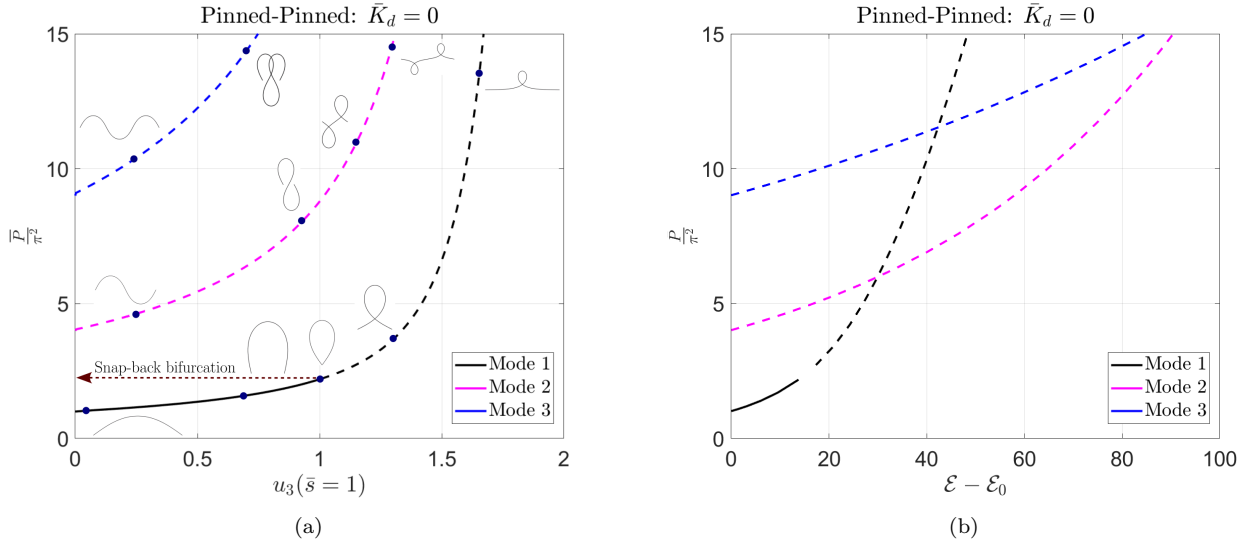


Fig. 9: Euler's Elastica: (a) Stability diagram (b) Total energy curve for pinned-pinned configuration; $\mathcal{E}_0 = 0$.

A close examination of Eqn. (27) reveals that under the transformation of θ , i.e., $\theta \rightarrow -\theta$, the equation possesses reflection symmetry if the condition $\bar{R} = 0$ is met. We observe that \bar{R} always remains zero for all \bar{P}_n ($n = 1, 2, \dots$) for pinned-pinned scenario. Nevertheless, for the fixed-fixed case, $\bar{R} = 0$ for odd n ($n = 1, 3, \dots$) while it is non-zero for even n . The corresponding rich bifurcation behaviour in Fig. 8a could be attributed to this change of symmetry.

5.2 Soft ferromagnetic ribbon: Transverse external magnetic field, $\bar{h}_e = e_2$

We recall the demag. energy in soft magnetic case is $K_d \text{at} \int (e_2 \cdot \mathbf{n})^2 ds$. To minimize the demag. energy, the curve's normal tends to align with the e_3 direction. This elongates the curve more in the e_2 direction. We consider $\bar{K}_d = 100$ for our analysis, since the magnetostatic energy becomes comparable to the mechanical energy in this regime.

Fig. 10a shows the stability diagram for fixed-free boundary condition ferromagnetic ribbon in the presence of a transverse \mathbf{h}_e external magnetic field, see Fig. 4. It is observed that the critical load here is tensile. The first nonlinear mode remains stable for all $\bar{P} > -197.53$ and this bifurcation is continuous.

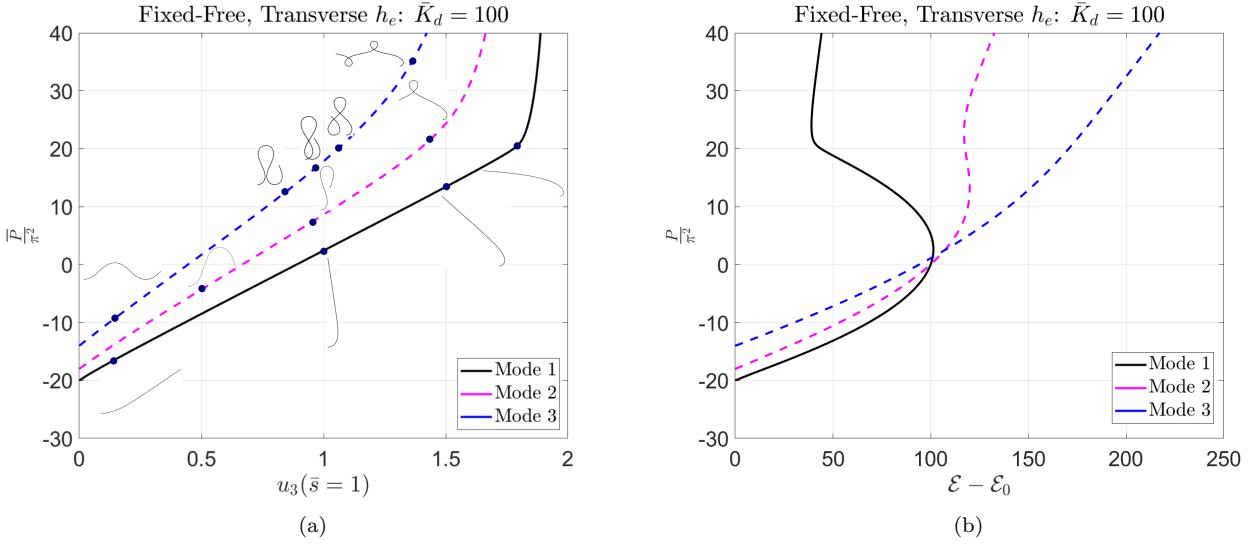


Fig. 10: Soft ferromagnetic ribbon, $\bar{K}_d = 100$: (a) Stability diagram, note that the first critical load is tensile, that is, $\bar{P}_1 = -20.01\pi^2$. (b) Total energy curve for fixed-free configuration under transverse magnetic field; $\mathcal{E}_0 = -100$.

For the fixed-fixed boundary condition, soft ferromagnetic ribbon buckles at a tensile load, and mode-1 deformation is observed for $\bar{P} > -160.52$, see Fig. 11. The ribbon snaps to the mode-2 branch as \bar{P} is increased as seen in Fig. 11. The ribbon deforms further along the mode-2 branch with gradual decrease in \bar{P} . As we unload, that is, decrease \bar{P} on the mode-2 branch, we observe the formation of new stable deformed configurations for tensile loads before it snaps back to the reference state. We observe a prolonged stretch of a stable segment in the mode-2 branch under the influence of \mathbf{h}_e for tensile loads ($\bar{P} < 0$). This stable segment persists even after the two supports have crossed each other significantly. Interestingly, we observe novel and stable states in this segment of the mode-2 branch. This segment is highlighted in Fig. 11a. We have highlighted one such novel and stable deformed configuration in red in Fig. 11a, when the end displacement is $u_3 = 0.65$. Note that in the deformed configuration depicted in red in Fig. 11a, there are two self-intersection points. A few intermediate novel deformed configurations are shown in red in Fig. 11b. Curves with two self-intersection points are not observed in any stable configuration in the purely elastic case. As \bar{P} is further reduced along this branch, that is, as we increase the tensile load, the ribbon undergoes a secondary bifurcation after which the ribbon snaps to the pre-buckled (reference) tensile configuration.

For the pinned-pinned soft ferromagnetic ribbon, the stability diagram Fig. 12a is qualitatively similar to the purely elastic case, except that the deformed shape is elongated along the e_2 direction and the critical load is tensile. Thus, for a soft ferromagnetic ribbon for all the boundary conditions, the critical load is tensile and they can be determined from linearized equations (Eqn. (24)) about $\theta(\bar{s}) \approx 0$ such that $\sin \theta(\bar{s}) \approx \theta(\bar{s})$ and $\cos \theta(\bar{s}) \approx 1$

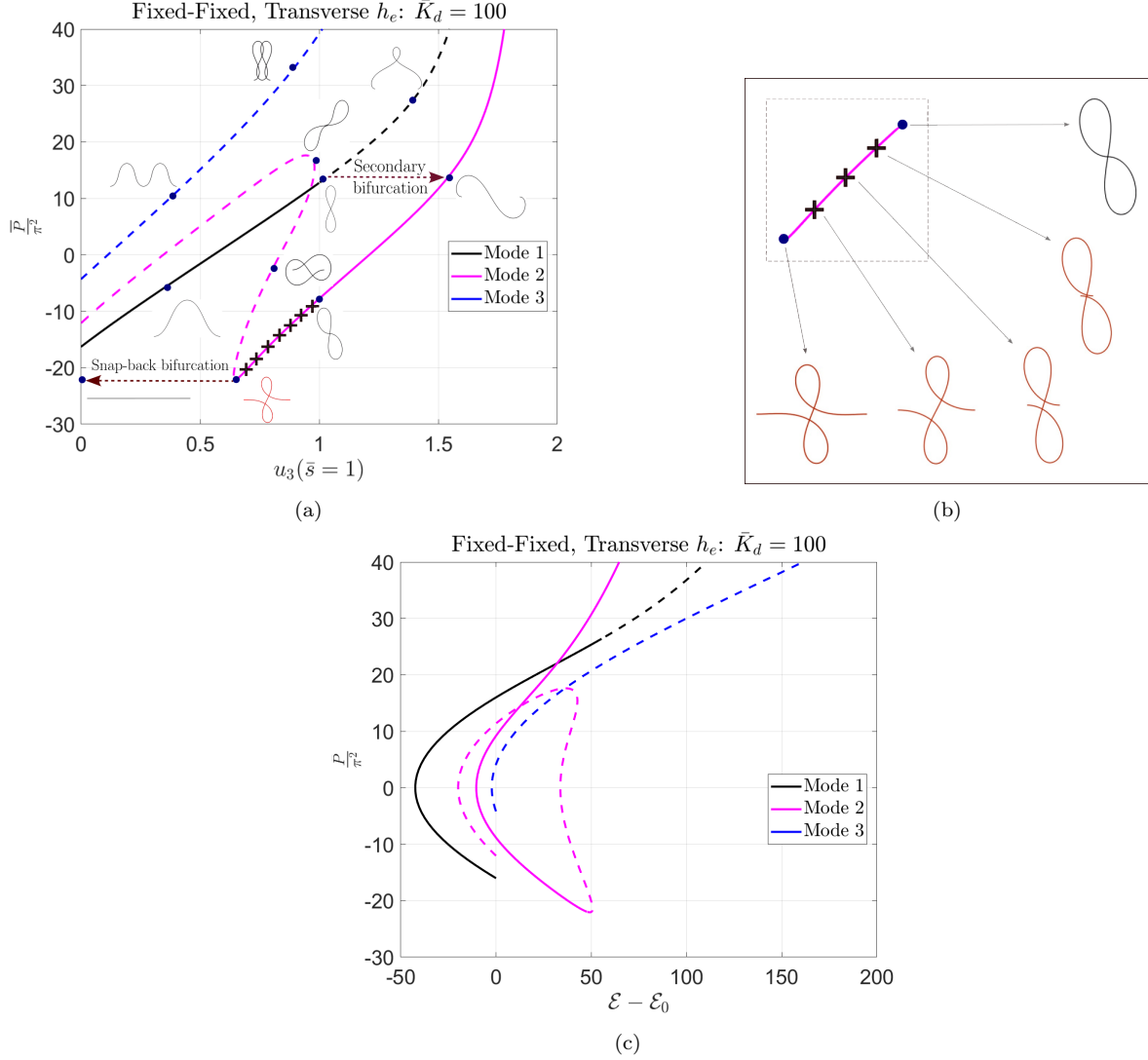


Fig. 11: Soft ferromagnetic ribbon, $\bar{K}_d = 100$: (a) Stability diagram, segment of the mode-2 branch corresponding to novel stable curves is highlighted in '+' symbol. Deformed config. shown in red represents one such novel stable curve on this segment that cannot be observed in purely elastic ribbon. (b) Segment of the mode-2 branch showing novel stable deformed configurations. (c) Total energy curve for fixed-fixed configuration under transverse magnetic field; $\mathcal{E}_0 = -100$.

as follows:

$$\theta''(\bar{s}) + (\bar{P} + 2\bar{K}_d)\theta(\bar{s}) + \bar{R} = 0, \quad (74)$$

subject to the integral constraint (for fixed-fixed and pinned conditions):

$$\bar{y}(1) = \int_0^1 \theta(\bar{s}) d\bar{s} = 0,$$

and gives the critical loads as

- fixed-free: $\bar{P}_n = \left(n - \frac{1}{2}\right)^2 \pi^2 - 2\bar{K}_d$, $n = 1, 2, \dots$,
- fixed-fixed: $2 \tan \frac{\sqrt{\bar{P}_n + 2\bar{K}_d}}{2} = \sqrt{\bar{P}_n + 2\bar{K}_d}$,
- pinned-pinned: $\bar{P}_n = n^2 \pi^2 - 2\bar{K}_d$.

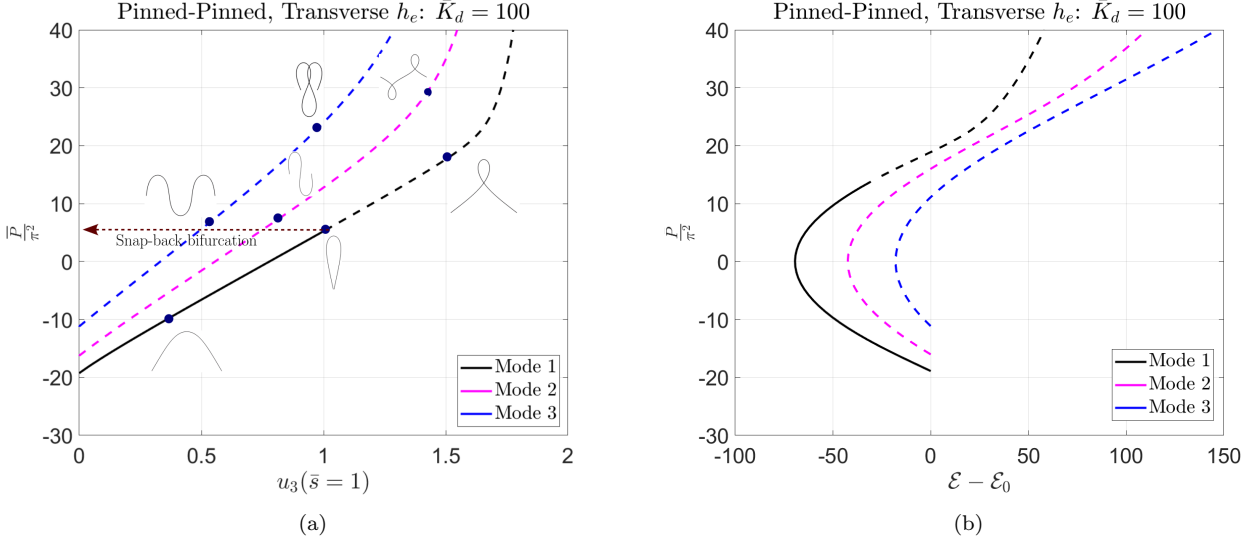


Fig. 12: Soft ferromagnetic ribbon, $\bar{K}_d = 100$: (a) Stability diagram (b) Total energy curve for pinned-pinned configuration under transverse magnetic field; $\mathcal{E}_0 = -100$.

5.3 Hard ferromagnetic ribbon

We now present our analysis for the hard ferromagnetic ribbon. Recall that, in this case that the magnetization vector makes a constant angle with the tangent at each point along the curve. Comparing Eqns. (30) and (27) reveals that, in this case, magnetization does not change the structure of Euler's Elastica equilibrium equations. The deformed configurations of Euler's Elastica corresponding to the hard magnetic case are obtained by a simple translation of the stability curves of those of Euler's Elastica (Figs. 7,8, 9) along \bar{P} -axis, see Figs. 13, 14 and 15. It is also noted that the equations for the cases – axial h_e , $\mathbf{m}(\bar{s}) = \mathbf{t}(\bar{s})$ and transverse h_e , $\mathbf{m}(\bar{s}) = \mathbf{n}(\bar{s})$ – coincide, thus leading to the same solutions. The critical loads significantly exceed those corresponding to the classical Elastica. This can easily be seen by linearizing Eqns. (30)₁ and (30)₄.

Our proposed model and results matches with the equilibrium equation for planar deformation of hard ferromagnetic ribbon under fixed-free configuration, as reported by Zhao et al [27] and Wang et al. [25,24], when only subjected to an external magnetic field and no mechanical load.

Axial external magnetic field h_e : Comparing equilibrium equation of the hard ferromagnetic ribbon with $\mathbf{m}(\bar{s}) = \mathbf{n}(\bar{s})$ (Eqn. (31)₂) and Eqn. (27) shows that in this case

$$\bar{Q} = \bar{R} + 2\bar{K}_d h_e. \quad (75)$$

Thus, the results are identical.

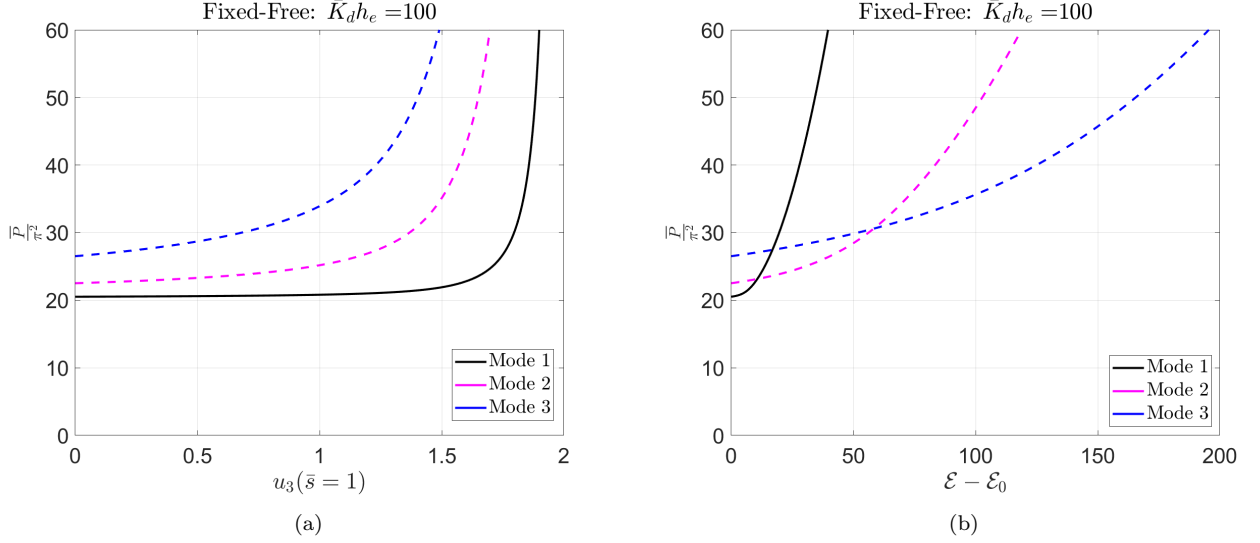


Fig. 13: Hard ferromagnetic ribbon: Axial h_e , Fixed-Free, $\mathbf{m} = \mathbf{t}(\bar{s})$, $\bar{K}_d h_e = 100$: (a) Stability diagram (b) Total energy curve; $\mathcal{E}_0 = 0$.

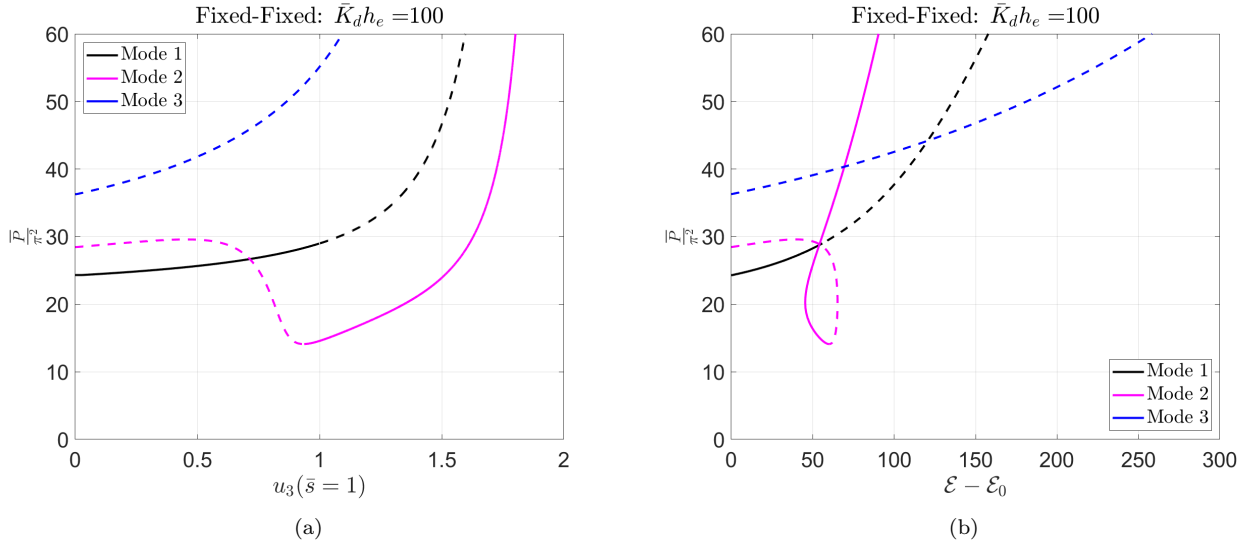


Fig. 14: Hard ferromagnetic ribbon: Axial h_e , Fixed-Fixed, $\mathbf{m} = \mathbf{t}(\bar{s})$, $\bar{K}_d h_e = 100$: (a) Stability diagram (b) Total energy curve; $\mathcal{E}_0 = 0$.

Transverse external magnetic field h_e : The deformed configurations of the hard ferromagnetic ribbon with tangential magnetization distribution, $\mathbf{m}(\bar{s}) = \mathbf{t}(\bar{s})$, are identical to the purely elastic counterpart. On matching the coefficients of Eqns. (30)₃ and (27), we arrive at the following relationship between the Lagrange multipliers \bar{R} and \bar{Q} :

$$\bar{Q} = \bar{R} - 2\bar{K}_d h_e. \quad (76)$$

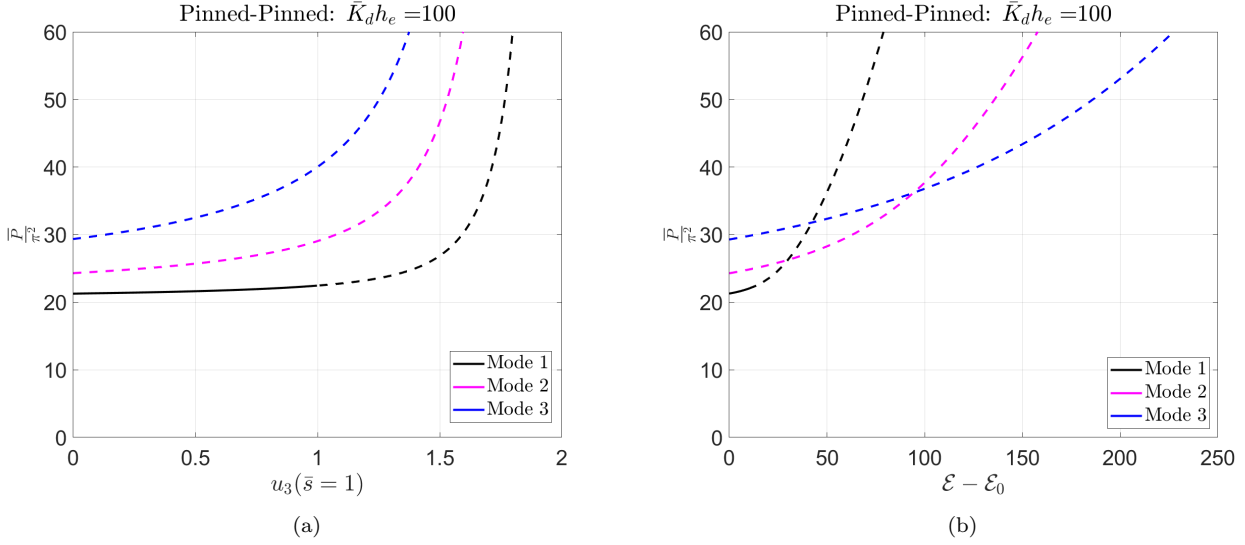


Fig. 15: Hard ferromagnetic ribbon: Axial h_e , Pinned-Pinned, $\mathbf{m} = \mathbf{t}(\bar{s})$, $\bar{K}_d h_e = 100$: (a) Stability diagram (b) Total energy curve; $\mathcal{E}_0 = 0$.

5.4 Limit as $\bar{K}_d \rightarrow \infty$

In this section, we explore the deformation of our planar ferromagnetic ribbons as the limit of $\bar{K}_d \rightarrow \infty$ approaches infinity. This limit is also attained when E , a , l , and K_d are held constant, and as $t \rightarrow 0$. This represents a physically relevant limit for nano rods/ribbons used in MEMS devices [22].

As $\bar{K}_d \rightarrow \infty$, the magnetostatic energy is much larger than the elastic energy. In this regime, the magnetization \mathbf{m} and the normal \mathbf{n} are perpendicular almost all along the length of the ribbon, except in short intervals where this condition cannot be met due to either the imposed mechanical boundary condition or due to the isoperimetric constraint imposed due to inextensibility. These short intervals exhibit a curvature with a radius denoted as r_c , see Fig. Fig. 16. An estimation of r_c can be obtained by balancing the elastic energy and demagnetization energy, as outlined below:

$$\begin{aligned} \text{Total energy : } & \frac{EI}{2} \int_0^l \kappa^2(s) ds + K_d a t \int_0^l (\mathbf{m} \cdot \mathbf{n})^2 ds \approx EI \int_0^{2\pi r} \frac{1}{r^2} ds + K_d a t \int_0^{2\pi r} ds \\ & = \frac{EI \cdot 2\pi}{r} + K_d a t \cdot 2\pi r. \end{aligned} \quad (77)$$

Optimising the total energy with respect to r , we obtain $r_c \sim \mathcal{O}\left(t\sqrt{\frac{E}{K_d}}\right)$. The deformed configurations in this regime of fixed-free, fixed-fixed, and pinned-pinned soft ferromagnetic ribbons are shown in Figure 16.

6 Conclusions

In this paper, we have presented a novel model that combines ideas from Euler's Elastica and continuum theory of micromagnetics to predict the deformation of ferromagnetic ribbons. We have analysed the buckling of a planar inextensible ribbon subjected to a large but constant external magnetic field and a gradually applied quasi-static load. While maintaining fixed magnetisation, we investigate the influence of magnetisation on the deformation of the planar ferromagnetic ribbon. Exploring how deformation influences magnetisation is an intriguing area for future

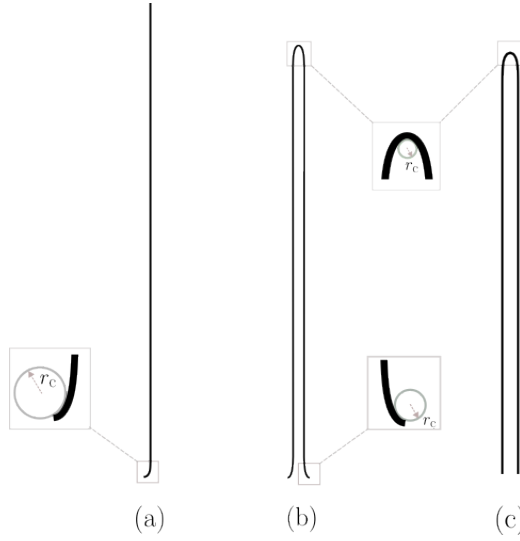


Fig. 16: Deformed shapes of soft ferromagnetic ribbon for $\bar{K}_d = 10^4$ showing osculating circles at the curved bends: (a) fixed-free (b) fixed-fixed, and (c) pinned-pinned cases.

research, although it presents a challenging problem. Our analysis commences by deriving and incorporating the magnetostatic energy of a curved structure into the total energy of the system. We derive the equilibrium equations and solve them numerically to obtain the equilibrium path as the load is increased. Further, we also determine the stability of the equilibrium solutions by casting the second variation of the total energy as a Sturm-Liouville eigenvalue problem, which is solved numerically.

We examine ribbons composed of both hard and soft ferromagnetic properties, exploring different orientations of externally applied magnetic fields and various mechanical boundary conditions. We observe that the critical buckling load is tensile mainly for a soft ferromagnetic ribbon under various canonical boundary conditions. Interestingly, our findings reveal the presence of novel stable configurations in the case of a fixed-fixed setup with a transversally applied external magnetic field. We anticipate that these stable configurations can be observed through meticulously conducted experiments.

Our analysis can be readily extended to understanding the deformation of planar ferromagnetic rods. The magnetostatic energy of planar ferromagnetic rod scales as $\mathcal{O}(K_d \pi r^2 l)$ [23]. A balance of the elastic energy $\mathcal{O}(E \pi (\frac{r^4}{8l}))$, and the magnetostatic energy for ferromagnetic rods would suggest that our analysis remains valid for rods with an aspect ratio of $\mathcal{O}\left(\sqrt{\frac{E}{8K_d}}\right)$.

The stability analysis conducted in our study solely examines planar perturbations. It is widely recognized that, in the case of Euler's Elastica, stability under planar perturbations does not guarantee stability of the equilibrium configurations under fully three-dimensional perturbations [18]. Motivated by this study, we outline the following future research directions:

- Explore stability under three-dimensional perturbations, and ascertain the potential role of the vertical reaction, \bar{R} , in this analysis.
- Investigating the influence of twist and out-of-plane deformation on ferromagnetic ribbons.
- Design laboratory experiments to observe novel stable deformed configurations of ferromagnetic ribbon structures, as identified in our analysis.

Acknowledgements We acknowledge Dr. Raghavendra Venkatraman (Courant Institute) for his valuable suggestions and insights on the draft of this paper. Furthermore, we would like to acknowledge the Indian Institute of Science Startup Grant and the Prime Minister's Research Fellowship (PMRF ID: 0201857) for providing financial support for this research.

Conflict of interest

The authors declare that they have no conflict of interest.

A Derivation of magnetostatic energy

In this section, we present the calculation of the leading order demag. energy of a deformed planar ferromagnetic ribbon. The magnetostatic energy is evaluated by solving Maxwell's equations of magnetostatics

$$\begin{aligned}\nabla \times \mathbf{h}_m(\mathbf{x}) &= 0, \\ \nabla \cdot (\mathbf{h}_m + \mathbf{m}(\mathbf{x})) &= 0.\end{aligned}\quad (78)$$

Applying Fourier transform to the above equations imply

$$\boldsymbol{\xi} \times \hat{\mathbf{h}}_m = 0, \quad (79)$$

$$\boldsymbol{\xi} \cdot (\hat{\mathbf{h}}_m + \hat{\mathbf{m}}) = 0, \quad (80)$$

where $\hat{\mathbf{f}}(\boldsymbol{\xi}) := \int_{\mathbb{R}^3} \mathbf{f}(\mathbf{x}) \exp(-i2\pi\mathbf{x} \cdot \boldsymbol{\xi}) d\mathbf{x}$. Eqn. (79) implies $\hat{\mathbf{h}}_m \parallel \boldsymbol{\xi}$ and hence,

$$\hat{\mathbf{h}}_m = (\hat{\mathbf{h}}_m \cdot \hat{\boldsymbol{\xi}}) \hat{\boldsymbol{\xi}} \text{ where } \hat{\boldsymbol{\xi}} = \frac{\boldsymbol{\xi}}{|\boldsymbol{\xi}|}. \quad (81)$$

Eqn. (80) implies that $\boldsymbol{\xi} \cdot \hat{\mathbf{h}}_m = -\boldsymbol{\xi} \cdot \hat{\mathbf{m}}$ and hence $\hat{\mathbf{h}}_m = -(\hat{\boldsymbol{\xi}} \cdot \hat{\mathbf{m}}) \hat{\boldsymbol{\xi}}$. Using Planchel's identity, we can then write the magnetostatic energy as follows

$$\int_{\mathbb{R}^3} |\mathbf{h}_m|^2 d\mathbf{x} = \int_{\mathbb{R}^3} |\hat{\mathbf{h}}_m|^2 d\boldsymbol{\xi} = \int_{\mathbb{R}^3} (\hat{\boldsymbol{\xi}} \cdot \hat{\mathbf{m}})^2 d\boldsymbol{\xi} = \int_{\mathbb{R}^3} \frac{(\boldsymbol{\xi} \cdot \hat{\mathbf{m}})^2}{|\boldsymbol{\xi}|^2} d\boldsymbol{\xi} = \int_{\mathbb{R}^3} \frac{|\widehat{\nabla \cdot \mathbf{m}}|^2}{|\boldsymbol{\xi}|^2} d\boldsymbol{\xi}. \quad (82)$$

We carry out the above integration in the material frame $(\mathbf{d}_1(s), \mathbf{d}_2(s), \mathbf{d}_3(s))$ and $\mathbf{x} \mapsto \mathbf{r}(s) + \tilde{a}\mathbf{d}_1(s) + \tilde{t}\mathbf{d}_2(s)$. The Fourier transform in the material frame is given as follows:

$$\mathcal{F}[\nabla \cdot \mathbf{m}](\boldsymbol{\xi}) = \widehat{\nabla \cdot \mathbf{m}}(\boldsymbol{\xi}) = \int_{\Omega} (\nabla \cdot \mathbf{m}) \exp(-i2\pi\mathbf{x} \cdot \boldsymbol{\xi}) d\mathbf{x} = \int_{\Omega} (\nabla \cdot \mathbf{m}) \exp(-i2\pi(\mathbf{r}(s) + \tilde{a}\mathbf{d}_1(s) + \tilde{t}\mathbf{d}_2(s)) \cdot \boldsymbol{\xi}) J ds d\tilde{t} d\tilde{a}, \quad (83)$$

here, $\mathcal{F}(v)$ denotes Fourier transform of v and $J = \left| \frac{\partial(x_1, x_2, x_3)}{\partial(s, \tilde{a}, \tilde{t})} \right|$ is the Jacobian associated with the change of variables. The divergence of \mathbf{m} is invariant upon coordinate transformation and is expressed as follows in the material frame:

$$\nabla \cdot \mathbf{m} = \frac{1}{h_s h_{\tilde{a}} h_{\tilde{t}}} \left\{ \frac{\partial(h_{\tilde{a}} h_{\tilde{t}} m_{d_3})}{\partial s} + \frac{\partial(h_{\tilde{t}} h_s m_{d_1})}{\partial \tilde{a}} + \frac{\partial(h_s h_{\tilde{a}} m_{d_2})}{\partial \tilde{t}} \right\}, \quad (84)$$

here, $h_s = \left| \frac{\partial \mathbf{x}}{\partial s} \right|$, $h_{\tilde{a}} = \left| \frac{\partial \mathbf{x}}{\partial \tilde{a}} \right|$ and $h_{\tilde{t}} = \left| \frac{\partial \mathbf{x}}{\partial \tilde{t}} \right|$.

Note:

$$\begin{aligned}-\frac{\partial \mathbf{x}}{\partial s} &= \mathbf{r}'(s) + \tilde{a}\mathbf{d}'_1(s) + \tilde{t}\mathbf{d}'_2(s) = \mathbf{d}_3(s) + \tilde{t}\kappa\mathbf{d}_3(s) = (1 + \tilde{t}\kappa)\mathbf{d}_3(s) \implies h_s = (1 + \tilde{t}\kappa), \\ -\frac{\partial \mathbf{x}}{\partial \tilde{a}} &= \mathbf{d}_1(s) \implies h_{\tilde{a}} = 1, \\ -\frac{\partial \mathbf{x}}{\partial \tilde{t}} &= \mathbf{d}_2(s) \implies h_{\tilde{t}} = 1.\end{aligned}$$

Furthermore, $J = h_s h_{\tilde{a}} h_{\tilde{t}}$, and hence

$$\begin{aligned}\nabla \cdot \mathbf{m} &= \frac{1}{J} \left\{ \frac{\partial m_{d_3}}{\partial s} + (1 + \tilde{t}\kappa) \frac{\partial m_{d_1}}{\partial \tilde{a}} + (1 + \tilde{t}\kappa) \frac{\partial m_{d_2}}{\partial \tilde{t}} + \kappa m_{d_2} \right\} \\ &= \frac{1}{J} \left\{ (\partial_{\tilde{a}} m_{d_1} + \partial_{\tilde{t}} m_{d_2} + \partial_s m_{d_3}) + \kappa(\tilde{t}\partial_{\tilde{a}} m_{d_1} + \tilde{t}\partial_{\tilde{t}} m_{d_2} + m_{d_2}) \right\}.\end{aligned}\quad (85)$$

Substituting the above expression for $\nabla \cdot \mathbf{m}$ in Eqn. (83) can now be written as follows:

$$\mathcal{F}[\nabla \cdot \mathbf{m}](\boldsymbol{\xi}) = \int_{\Omega} \frac{1}{J} \left\{ (\partial_{\tilde{a}} m_{d_1} + \partial_{\tilde{t}} m_{d_2} + \partial_s m_{d_3}) + \kappa(\tilde{t}\partial_{\tilde{a}} m_{d_1} + \tilde{t}\partial_{\tilde{t}} m_{d_2} + m_{d_2}) \right\} \exp(-i2\pi(\mathbf{r}(s) + \tilde{a}\mathbf{d}_1(s) + \tilde{t}\mathbf{d}_2(s)) \cdot \boldsymbol{\xi}) J ds d\tilde{t} d\tilde{a}. \quad (86)$$

Since $\mathbf{r}(0) = \mathbf{0}$ and $\mathbf{r}(s) \cdot \boldsymbol{\xi} = \int_0^s \mathbf{d}_3(s') ds' \cdot \boldsymbol{\xi} = s\xi_{d_3}$ and therefore, $(\mathbf{r}(s) + \tilde{a}\mathbf{d}_1(s) + \tilde{t}\mathbf{d}_2(s)) \cdot \boldsymbol{\xi} = \tilde{a}\xi_{d_1} + \tilde{t}\xi_{d_2} + s\xi_{d_3}$. The divergence of \mathbf{m} in the material frame is written as a sum of these six integrals:

$$\mathcal{F}[\nabla \cdot \mathbf{m}](\boldsymbol{\xi}) = I_1 + I_2 + I_3 + I_4 + I_5 + I_6, \quad (87)$$

where

$$\begin{aligned} I_1 &= \mathcal{F}[\partial_{\tilde{a}} m_{d_1}](\boldsymbol{\xi}_d) = \xi_{d_1} F_0(a, \xi_{d_1}) F_0(t, \xi_{d_2}) \mathcal{F}[m_{d_1} \chi_{(0,l)}(s)](\xi_{d_3}) \quad (\text{even in } \xi_{d_2}), \\ I_2 &= \mathcal{F}[\partial_{\tilde{t}} m_{d_2}](\boldsymbol{\xi}_d) = \xi_{d_2} F_0(a, \xi_{d_1}) F_0(t, \xi_{d_2}) \mathcal{F}[m_{d_2} \chi_{(0,l)}(s)](\xi_{d_3}) \quad (\text{odd in } \xi_{d_2}), \\ I_3 &= \mathcal{F}[\partial_s m_{d_3}](\boldsymbol{\xi}_d) = F_0(a, \xi_{d_1}) F_0(t, \xi_{d_2}) \mathcal{F}[\partial_s m_{d_3} \chi_{(0,l)}(s)](\xi_{d_3}) \quad (\text{even in } \xi_{d_2}), \\ I_4 &= \mathcal{F}[\kappa \tilde{t} \partial_{\tilde{a}} m_{d_1}](\boldsymbol{\xi}_d) = \xi_{d_1} F_0(a, \xi_{d_1}) F_1(t, \xi_{d_2}) \mathcal{F}[\kappa m_{d_1} \chi_{(0,l)}(s)](\xi_{d_3}) \quad (\text{odd in } \xi_{d_2}), \\ I_5 &= \mathcal{F}[\kappa \tilde{t} \partial_{\tilde{t}} m_{d_2}](\boldsymbol{\xi}_d) = F_0(a, \xi_{d_1}) \xi_{d_2} F_1(t, \xi_{d_2}) \mathcal{F}[\kappa m_{d_2} \chi_{(0,l)}(s)](\xi_{d_3}) \quad (\text{even in } \xi_{d_2}), \\ I_6 &= \mathcal{F}[\kappa m_{d_2}](\boldsymbol{\xi}_d) = F_0(a, \xi_{d_1}) F_1(t, \xi_{d_2}) \mathcal{F}[\kappa m_{d_2} \chi_{(0,l)}(s)](\xi_{d_3}) \quad (\text{even in } \xi_{d_2}), \end{aligned} \quad (88)$$

where $F_0(v, \eta)$ and $F_1(v, \eta)$ are defined as follows:

$$F_0(v, \eta) = \int_{-v/2}^{v/2} \exp(-i2\pi\eta v') dv' \quad \text{and} \quad F_1(v, \eta) = \int_{-v/2}^{v/2} v' \exp(-i2\pi\eta v') dv'.$$

The magnetostatic energy can now be expressed in terms of $I_1, I_2, I_3, I_4, I_5, I_6$ as follows:

$$\begin{aligned} \int_{\mathbb{R}^3} \frac{|\widehat{\nabla \cdot \mathbf{m}}(\boldsymbol{\xi}_d)|^2}{|\boldsymbol{\xi}_d|^2} d\boldsymbol{\xi}_d &= \int_{\mathbb{R}^3} \frac{(I_1 + I_2 + I_3 + I_4 + I_5 + I_6)^2}{|\boldsymbol{\xi}_d|^2} \\ &= \underbrace{\int \frac{I_1^2}{|\boldsymbol{\xi}_d|^2}}_{\mathcal{O}(t^2)} + \underbrace{\int \frac{I_2^2}{|\boldsymbol{\xi}_d|^2}}_{\mathcal{O}(t)} + \underbrace{\int \frac{I_3^2}{|\boldsymbol{\xi}_d|^2}}_{\mathcal{O}(t^2)} + \underbrace{\int \frac{I_4^2}{|\boldsymbol{\xi}_d|^2}}_{\mathcal{O}(t^5)} + \underbrace{\int \frac{I_5^2}{|\boldsymbol{\xi}_d|^2}}_{\mathcal{O}(t^3)} + \underbrace{\int \frac{I_6^2}{|\boldsymbol{\xi}_d|^2}}_{\mathcal{O}(t^3)} \\ &\quad + 2 \underbrace{\int \frac{I_1 I_3}{|\boldsymbol{\xi}_d|^2}}_{\mathcal{O}(t^2)} + 2 \underbrace{\int \frac{I_1 I_5}{|\boldsymbol{\xi}_d|^2}}_{\mathcal{O}(t^3)} + 2 \underbrace{\int \frac{I_1 I_6}{|\boldsymbol{\xi}_d|^2}}_{\mathcal{O}(t^2)} + 2 \underbrace{\int \frac{I_2 I_4}{|\boldsymbol{\xi}_d|^2}}_{\mathcal{O}(t^3)} + 2 \underbrace{\int \frac{I_3 I_5}{|\boldsymbol{\xi}_d|^2}}_{\mathcal{O}(t^3)} + 2 \underbrace{\int \frac{I_3 I_6}{|\boldsymbol{\xi}_d|^2}}_{\mathcal{O}(t^2)} + 2 \underbrace{\int \frac{I_5 I_6}{|\boldsymbol{\xi}_d|^2}}_{\mathcal{O}(t^3)}. \end{aligned} \quad (89)$$

The remaining product terms are odd functions in ξ_{d_2} and hence they integrate out to zero. Therefore we have the leading order term for the magnetostatic energy as follows:

$$\int_{\mathbb{R}^3} \frac{|\widehat{\nabla \cdot \mathbf{m}}(\boldsymbol{\xi}_d)|^2}{|\boldsymbol{\xi}_d|^2} d\boldsymbol{\xi}_d = \int_{\mathbb{R}^3} \frac{I_2^2}{|\boldsymbol{\xi}_d|^2} d\boldsymbol{\xi}_d + \mathcal{O}(t^2). \quad (90)$$

Now,

$$\lim_{t \rightarrow 0} \int_{\mathbb{R}^3} \frac{I_2^2}{|\boldsymbol{\xi}_d|^2} d\boldsymbol{\xi}_d = at \int_{\mathbb{R}} \widehat{m}_{d_2}(\xi_{d_3}) d\xi_{d_3} + \mathcal{O}(t^2) = at \int_{s=0}^l (m_{d_2})^2 ds + \mathcal{O}(t^2). \quad (91)$$

Hence, we have

$$\int_{\mathbb{R}^3} |\mathbf{h}_m|^2 d\mathbf{x} = at \int_{s=0}^l (m_{d_2})^2 ds + \mathcal{O}(t^2). \quad (92)$$

B Numerical discretization of equilibrium equations

We demonstrate the discretization process for Eqn. (24) invoking fixed-fixed boundary conditions. We discretize the domain into $N + 1$ nodal points as $\bar{s}_i = ih; i = 0, 1, \dots, N + 1$ where $h = \frac{l}{N+1}$. We utilize second-order accurate central difference scheme to approximate the second-order derivative in Eqn. (24). The discrete system of equations alongwith the boundary conditions is

$$\begin{aligned} \frac{\theta_{i-1} - 2\theta_i + \theta_{i+1}}{h^2} + \bar{P} \sin \theta_i + \bar{K}_d \sin 2\theta_i + \bar{R} \cos \theta_i &= 0; \quad i = 1, 2, \dots, N, \\ \theta_0 = 0, \theta_{N+1} &= 0, \end{aligned} \quad (93)$$

Integrating by parts the first term,

$$\delta^2 \bar{\mathcal{E}}(\theta) = \underbrace{\eta' \eta \Big|_0^1}_{=0} - \int_0^1 \eta'' \eta d\bar{s} - 2\bar{K}_d \int_0^1 \cos 2\theta \eta^2 d\bar{s} - \bar{P} \int_0^1 \cos \theta \eta^2 d\bar{s} + \bar{R} \int_0^1 \sin \theta \eta^2 d\bar{s}, \quad (103)$$

$$\implies \delta^2 \bar{\mathcal{E}}(\theta) = - \int_0^1 [\eta'' + 2\bar{K}_d \cos 2\theta \eta + \bar{P} \cos \theta \eta - \bar{R} \sin \theta \eta] \eta d\bar{s}, \quad (104)$$

for all kinematically admissible functions $\eta(\bar{s})$. The stability criterion requires that

$$\delta^2 \bar{\mathcal{E}}(\theta) \begin{cases} > 0 & \text{stable} \\ < 0 & \text{unstable.} \end{cases} \quad (105)$$

Introducing first variation to the integral constraint $\int_0^1 \sin \theta(\bar{s}) d\bar{s} = 0$ results in

$$\int_0^1 \cos \theta(\bar{s}) \eta(\bar{s}) d\bar{s} = 0. \quad (106)$$

C.2 Construction of Sturm-Liouville problem

A meticulous study of the second variation $\delta^2 \bar{\mathcal{E}}(\theta)$ necessitates the construction of the following Sturm-Liouville problem whose non-trivial solutions are $\phi_n(\bar{s})$:

$$\phi_n''(\bar{s}) + \lambda_n (2\bar{K}_d \cos 2\theta + \bar{P} \cos \theta - \bar{R} \sin \theta) \phi_n(\bar{s}) = C_{R_n} \cos \theta(\bar{s}), \quad (107)$$

where λ_n are the eigenvalues, ϕ_n the corresponding eigenmodes of Eqn. (107) and $L(\bar{s}) = (2\bar{K}_d \cos 2\theta + \bar{P} \cos \theta - \bar{R} \sin \theta)$ denotes the weight function. C_{R_n} is meant to enforce the isoperimetric constraint (Eqn. (106)). The conditions on $\phi_n(\bar{s})$ are

- fixed-fixed case: $\phi_n(0) = \phi_n(1) = 0$ and $\int_0^1 \cos \theta(\bar{s}) \phi_n(\bar{s}) d\bar{s} = 0$,
- pinned-pinned case: $\phi_n'(0) = \phi_n'(1) = 0$ and $\int_0^1 \cos \theta(\bar{s}) \phi_n(\bar{s}) d\bar{s} = 0$,
- fixed-free case: $\phi_n(0) = \phi_n'(1) = 0$.

Multiplying both sides of Eqn. (107) by ϕ_n , integrating over the domain and using the conditions stipulated on $\phi_n(\bar{s})$, we get

$$\begin{aligned} \int_0^1 [\phi_n''(\bar{s}) + \lambda_n L(\bar{s})] \phi_n d\bar{s} &= C_{R_n} \underbrace{\int_0^1 \cos \theta(\bar{s}) \phi_n d\bar{s}}_0, \\ \implies \lambda_n \int_0^1 L(\bar{s}) \phi_n^2 d\bar{s} &= \int_0^1 \phi_n'^2 d\bar{s}. \end{aligned} \quad (108)$$

We multiply Eqn. (107) by ϕ_m and integrate over the domain to get

$$\begin{aligned} \int_0^1 [\phi_n''(\bar{s}) + \lambda_n L(\bar{s}) \phi_n(\bar{s})] \phi_m d\bar{s} &= C_{R_n} \underbrace{\int_0^1 \cos \theta(\bar{s}) \phi_m d\bar{s}}_0, \\ \implies - \int_0^1 \phi_n' \phi_m' d\bar{s} + \lambda_n \int_0^1 L(\bar{s}) \phi_n \phi_m d\bar{s} &= 0. \end{aligned} \quad (109)$$

Similarly, consider Eqn. (55) for ϕ_m , multiply it by ϕ_n and integrate by parts to get

$$- \int_0^1 \phi_m' \phi_n' d\bar{s} + \lambda_m \int_0^1 L(\bar{s}) \phi_n \phi_m d\bar{s} = 0. \quad (110)$$

Subtracting the second equation from the first results in

$$(\lambda_n - \lambda_m) \int_0^1 L(\bar{s}) \phi_n \phi_m d\bar{s} = 0. \quad (111)$$

For $n \neq m$, $\lambda_n \neq \lambda_m$, we obtain the orthogonality condition as

$$\int_0^1 L(\bar{s}) \phi_n \phi_m d\bar{s} = 0. \quad (112)$$

Spectral decomposition Let us use $\phi_n(\bar{s})$ alongwith the weight function $L(\bar{s})$ to construct a Fourier series representation (converging in the mean) to the square-integrable function $\eta(\bar{s})$,

$$\eta(\bar{s}) = \sum_{n=1}^{\infty} c_n \phi_n(\bar{s}), \quad c_n \text{ are Fourier coefficients.} \quad (113)$$

Substitute the above representation in Eqn. (104),

$$\begin{aligned} \delta^2 \bar{\mathcal{E}}(\theta) &= - \int_0^1 [c_n \phi_n'' + L(\bar{s}) c_n \phi_n] c_m \phi_m d\bar{s} \\ &= -c_m c_n \int_0^1 [C_{R_n} \cos \theta - \lambda_n L(\bar{s}) \phi_n(\bar{s})] \phi_m(\bar{s}) d\bar{s} - c_n c_m \int_0^1 L(\bar{s}) \phi_m(\bar{s}) \phi_n(\bar{s}) d\bar{s} \\ &= -c_m c_n C_{R_n} \underbrace{\int_0^1 \cos \theta \phi_m(\bar{s}) d\bar{s}}_{=0} + c_n c_m (\lambda_n - 1) \underbrace{\int_0^1 L(\bar{s}) \phi_m(\bar{s}) \phi_n(\bar{s}) d\bar{s}}_{\text{(use orthogonality condition)}} \\ &= c_n^2 (\lambda_n - 1) \int_0^1 L(\bar{s}) \phi_n^2(\bar{s}) d\bar{s} \\ &= c_n^2 (\lambda_n - 1) \frac{1}{\lambda_n} \int_0^1 (\phi_n'(\bar{s}))^2 d\bar{s}. \end{aligned}$$

The stability criterion is

$$\Rightarrow \delta^2 \bar{\mathcal{E}}(\theta) = \sum_{n=1}^{\infty} c_n^2 \left(1 - \frac{1}{\lambda_n}\right) \int_0^1 (\phi_n'(\bar{s}))^2 d\bar{s} \quad \begin{cases} > 0 \text{ if } \lambda_n \notin [0, 1] & \text{stable} \\ < 0 \text{ if } \lambda_n \in [0, 1] & \text{unstable.} \end{cases} \quad (114)$$

References

- Armanini, C., Dal Corso, F., Misseroni, D., Bigoni, D.: From the elastica compass to the elastica catapult: an essay on the mechanics of soft robot arm. *Proceedings of the Royal Society A: Mathematical, Physical and Engineering Sciences* **473**(2198), 20160870 (2017)
- Audoly, B., Pomeau, Y.: *Elasticity and Geometry: From Hair Curls to the Non-linear Response of Shells*. OUP Oxford (2010). URL <https://books.google.co.in/books?id=FMQRDAAAQBAJ>
- Balaeff, A., Mahadevan, L., Schulten, K.: Modeling dna loops using the theory of elasticity. *Physical Review E* **73**(3), 031919 (2006)
- Bigoni, D., Bosi, F., Misseroni, D., Corso, F.D., Noselli, G.: New phenomena in nonlinear elastic structures: from tensile buckling to configurational forces. In: *CISM International Centre for Mechanical Sciences*, pp. 55–135. Springer Vienna (2015). DOI 10.1007/978-3-7091-1877-1_2. URL https://doi.org/10.1007/978-3-7091-1877-1_2
- Coyne, J.: Analysis of the formation and elimination of loops in twisted cable. *IEEE Journal of Oceanic Engineering* **15**(2), 72–83 (1990)
- Dabade, V., Venkatraman, R., James, R.D.: Micromagnetics of galfenol. *Journal of Nonlinear Science* **29**(2), 415–460 (2018). DOI 10.1007/s00332-018-9492-8. URL <http://dx.doi.org/10.1007/s00332-018-9492-8>
- Dabade, V., Venkatraman, R., James, R.D.: Micromagnetics of galfenol. *Journal of Nonlinear Science* **29**, 415–460 (2019)
- DeSimone, A., Kohn, R.V., Müller, S., Otto, F.: A reduced theory for thin-film micromagnetics. *Communications on Pure and Applied Mathematics: A Journal Issued by the Courant Institute of Mathematical Sciences* **55**(11), 1408–1460 (2002)
- Doedel, E., Keller, H.B., Kernevez, J.P.: Numerical analysis and control of bifurcation problems: (i) bifurcation in finite dimensions. *International Journal of Bifurcation and Chaos* **01**(03), 493–520 (1991). DOI 10.1142/s0218127491000397. URL <https://doi.org/10.1142/s0218127491000397>
- Doedel, E., Keller, H.B., Kernevez, J.P.: Numerical analysis and control of bifurcation problems: (i) bifurcation in infinite dimensions. *International Journal of Bifurcation and Chaos* **01**(04), 745–772 (1991). DOI 10.1142/s0218127491000555. URL <https://doi.org/10.1142/s0218127491000555>
- Handral, P., Rangarajan, R.: An elastica robot: Tip-control in tendon-actuated elastic arms. *Extreme Mechanics Letters* **34**, 100584 (2020)
- James, R.: Configurational forces in magnetism with application to the dynamics of a small-scale ferromagnetic shape memory cantilever. *Continuum Mechanics and Thermodynamics* **14**(1), 55–86 (2002). DOI 10.1007/s001610100072. URL <http://dx.doi.org/10.1007/s001610100072>
- Keip, M.A., Sridhar, A.: A variationally consistent phase-field approach for micro-magnetic domain evolution at finite deformations. *Journal of the Mechanics and Physics of Solids* **125**, 805–824 (2019). DOI 10.1016/j.jmps.2018.11.012. URL <http://dx.doi.org/10.1016/j.jmps.2018.11.012>

14. Kim, Y., Parada, G.A., Liu, S., Zhao, X.: Ferromagnetic soft continuum robots. *Science Robotics* **4**(33), eaax7329 (2019)
15. Kuznetsov, V., Levyakov, S.: Complete solution of the stability problem for elastica of euler's column. *International journal of non-linear mechanics* **37**(6), 1003–1009 (2002)
16. Levyakov, S.V., Kuznetsov, V.V.: Stability analysis of planar equilibrium configurations of elastic rods subjected to end loads. *Acta Mechanica* **211**(1–2), 73–87 (2009). DOI 10.1007/s00707-009-0213-0. URL <http://dx.doi.org/10.1007/s00707-009-0213-0>
17. Maddocks, J.: Stability of nonlinearly elastic rods. *Archive for rational mechanics and analysis* **85**(4), 311–354 (1984)
18. Maddocks, J.H.: Stability of nonlinearly elastic rods. *Archive for Rational Mechanics and Analysis* **85**(4), 311–354 (1984). DOI 10.1007/bf00275737. URL <http://dx.doi.org/10.1007/BF00275737>
19. Peletan, L., Bague, S., Torkhani, M., Jacquet-Richardet, G.: Quasi-periodic harmonic balance method for rubbing self-induced vibrations in rotor–stator dynamics. *Nonlinear Dynamics* **78**(4), 2501–2515 (2014). DOI 10.1007/s11071-014-1606-8. URL <https://doi.org/10.1007/s11071-014-1606-8>
20. Pressley, A.: *Elementary Differential Geometry*. Springer London (2010). DOI 10.1007/978-1-84882-891-9. URL <https://doi.org/10.1007/978-1-84882-891-9>
21. Ramachandran, V., Bartlett, M.D., Wissman, J., Majidi, C.: Elastic instabilities of a ferroelastomer beam for soft reconfigurable electronics. *Extreme Mechanics Letters* **9**, 282–290 (2016). DOI 10.1016/j.eml.2016.08.007. URL <https://doi.org/10.1016/j.eml.2016.08.007>
22. Samy, O., Otsuji, T., El Moutaouakil, A.: Terahertz absorptance in mos2/graphene nanoribbon heterostructures. In: 2023 Photonics Electromagnetics Research Symposium (PIERS). IEEE (2023). DOI 10.1109/piers59004.2023.10221462. URL <http://dx.doi.org/10.1109/PIERS59004.2023.10221462>
23. Slastikov, V.V., Sonnenberg, C.: Reduced models for ferromagnetic nanowires. *IMA Journal of Applied Mathematics* **77**(2), 220–235 (2011). DOI 10.1093/imamat/hxr019. URL <https://doi.org/10.1093/imamat/hxr019>
24. Wang, L., Guo, C.F., Zhao, X.: Magnetic soft continuum robots with contact forces. *Extreme Mechanics Letters* **51**, 101604 (2022). DOI <https://doi.org/10.1016/j.eml.2022.101604>. URL <https://www.sciencedirect.com/science/article/pii/S2352431622000013>
25. Wang, L., Kim, Y., Guo, C.F., Zhao, X.: Hard-magnetic elastica. *Journal of the Mechanics and Physics of Solids* **142**, 104045 (2020). DOI <https://doi.org/10.1016/j.jmps.2020.104045>. URL <https://www.sciencedirect.com/science/article/pii/S0022509620302805>
26. Woodson, H.H., Melcher, J.R.: *Electromechanical Dynamics*, p. 634. Wiley (1985). URL <https://ocw.mit.edu/courses/res-6-003-electromechanical-dynamics-spring-2009/>
27. Zhao, R., Kim, Y., Chester, S.A., Sharma, P., Zhao, X.: Mechanics of hard-magnetic soft materials. *Journal of the Mechanics and Physics of Solids* **124**, 244–263 (2019). DOI 10.1016/j.jmps.2018.10.008. URL <https://doi.org/10.1016/j.jmps.2018.10.008>